

SOURCE AND PATH CALIBRATION IN REGIONS OF POOR CRUSTAL PROPAGATION USING TEMPORARY, LARGE-APERTURE, HIGH- RESOLUTION SEISMIC ARRAYS

John L. Nabelek, et al.

**Oregon State University
312 Kerr Admin. Bldg.
Corvallis, OR 97330-8507**

6 September 2013

Final Report

APPROVED FOR PUBLIC RELEASE; DISTRIBUTION IS UNLIMITED.



**AIR FORCE RESEARCH LABORATORY
Space Vehicles Directorate
3550 Aberdeen Ave SE
AIR FORCE MATERIEL COMMAND
KIRTLAND AIR FORCE BASE, NM 87117-5776**

DTIC COPY

NOTICE AND SIGNATURE PAGE

Using Government drawings, specifications, or other data included in this document for any purpose other than Government procurement does not in any way obligate the U.S. Government. The fact that the Government formulated or supplied the drawings, specifications, or other data does not license the holder or any other person or corporation; or convey any rights or permission to manufacture, use, or sell any patented invention that may relate to them.

This report was cleared for public release by the 377 ABW Public Affairs Office and is available to the general public, including foreign nationals. Copies may be obtained from the Defense Technical Information Center (DTIC) (<http://www.dtic.mil>).

AFRL-RV-PS-TR-2013-0139 HAS BEEN REVIEWED AND IS APPROVED FOR PUBLICATION IN ACCORDANCE WITH ASSIGNED DISTRIBUTION STATEMENT.

//SIGNED//

Robert Raistrick
Project Manager, AFRL/RVBYE

//SIGNED//

Edward J. Masterson, Colonel, USAF
Chief, Battlespace Environment Division

This report is published in the interest of scientific and technical information exchange, and its publication does not constitute the Government's approval or disapproval of its ideas or findings.

REPORT DOCUMENTATION PAGE				Form Approved OMB No. 0704-0188	
Public reporting burden for this collection of information is estimated to average 1 hour per response, including the time for reviewing instructions, searching existing data sources, gathering and maintaining the data needed, and completing and reviewing this collection of information. Send comments regarding this burden estimate or any other aspect of this collection of information, including suggestions for reducing this burden to Department of Defense, Washington Headquarters Services, Directorate for Information Operations and Reports (0704-0188), 1215 Jefferson Davis Highway, Suite 1204, Arlington, VA 22202-4302. Respondents should be aware that notwithstanding any other provision of law, no person shall be subject to any penalty for failing to comply with a collection of information if it does not display a currently valid OMB control number. PLEASE DO NOT RETURN YOUR FORM TO THE ABOVE ADDRESS.					
1. REPORT DATE (DD-MM-YYYY) 06-09-2013		2. REPORT TYPE Final Report		3. DATES COVERED (From - To) 17 Apr 2009 to 02 Apr 2013	
4. TITLE AND SUBTITLE Source and Path Calibration in Regions of Poor Crustal Propagation Using Temporary, Large-Aperture, High-Resolution Seismic Arrays				5a. CONTRACT NUMBER FA8718-09-C-0004	
				5b. GRANT NUMBER	
				5c. PROGRAM ELEMENT NUMBER 62601F	
6. AUTHOR(S) John L. Nabelek, Jochen Braunmiller, and W. Scott Phillips*				5d. PROJECT NUMBER 1010	
				5e. TASK NUMBER PPM00004803	
				5f. WORK UNIT NUMBER EF004078	
7. PERFORMING ORGANIZATION NAME(S) AND ADDRESS(ES) Oregon State University 312 Kerr Admin. Bldg. Corvallis, OR 97330-8507				8. PERFORMING ORGANIZATION REPORT NUMBER *Los Alamos National Laboratory PO Box 1663 Los Alamos, NM 87545	
9. SPONSORING / MONITORING AGENCY NAME(S) AND ADDRESS(ES) Air Force Research Laboratory Space Vehicles Directorate 3550 Aberdeen Avenue SE Kirtland AFB, NM 87117-5776				10. SPONSOR/MONITOR'S ACRONYM(S) AFRL/RVBYE	
				11. SPONSOR/MONITOR'S REPORT NUMBER(S) AFRL-RV-PS-TR-2013-0139	
12. DISTRIBUTION / AVAILABILITY STATEMENT Approved for public release; distribution is unlimited. (377ABW-2013-0938 dtd 28 Oct 2013)					
13. SUPPLEMENTARY NOTES					
14. ABSTRACT Broadband seismic data acquired during the Hi-CLIMB experiment are used to study seismic events and path propagation in the Nepal Himalaya and the south-central Tibetan Plateau. The 2002–2005 experiment consisted of 233 stations extending from the Himalayan foreland into the central Tibetan Plateau. The dataset provides an opportunity to obtain accurate seismic event locations for ground truth evaluation and to determine source moment-tensor parameters from waveform modeling.					
15. SUBJECT TERMS Hi-CLIMB, Ground Truth, Moment Tensors					
16. SECURITY CLASSIFICATION OF:			17. LIMITATION OF ABSTRACT	18. NUMBER OF PAGES	19a. NAME OF RESPONSIBLE PERSON
a. REPORT Unclassified	b. ABSTRACT Unclassified	c. THIS PAGE Unclassified			Robert Raistrick
			Unlimited	40	19b. TELEPHONE NUMBER (include area code)

This page is intentionally left blank.

Table of Contents

1. Summary	1
2. Introduction.....	1
3. The Hi-CLIMB Dataset	1
4. Seismic Event Location	3
4.1. Event Detection and Initial Location	3
4.2. Polarization S-Picker	7
4.3. $M_L(P)$	14
5. Source Parameters from Regional Moment Tensors	16
6. Published Results and Ongoing Research.....	21
6.1. Low-Angle Normal Faulting in the PXR.....	21
6.2. Velocity and Attenuation Tomography	23
7. GT5 Dataset	24
8. Conclusions.....	27
References.....	28
List of Symbols, Abbreviations, and Acronyms.....	30

List of Figures

1. Map of the Hi-CLIMB seismic network (phase-2: red triangles, phase-1: open triangles) and permanent GSN station Lhasa.....	2
2. Event detection for a 20-minute Hi-CLIMB data window (Julian day 193, 2004, start at 23:33 UTC).	3
3. Simplified flowchart of database post-processing steps performed to clean up the initial associated event table.....	4
4. Right. Observed (dots) and predicted (green lines) travel times vs. distance from the epicenter for a manually picked PXR event.	
4. Left. Refined velocity model tib3p based on these observations was used for final location of the Hi-CLIMB dataset.	5
5. Differences between manually and automatically picked arrival times for 16 stronger regional events.	6
6. Left. Map of 7,900+ events with at least 25 P and S picks shows high-quality locations with distinct clustering.	
6. Right. Requiring $D_{\min} \leq 50$ km, $\text{gap} \leq 225^\circ$, and $M_L \geq 2.0$ results in ~600 events with well-constrained depth.	7
7. Step-by-step process for S picking by polarization method for station H1400, 108 km from the 3 July 2005 $M_L(P)=3.0$ earthquake at 31.55°N and 85.62°E	9
8. Examples of S-phase picks with increasing distance, from 65 to 255 km, for same event as in Figure 7.....	11
9. Polarization (red) vs. STA/LTA (green) S picks for the 15 July 2004 $M_L(P)=2.9$ earthquake (30.66°N , 83.83°E).....	11
10. S-wave travel times vs. distance for small ($2.0 \leq M_L(P) \leq 2.7$) seismic events shown with 3.5 km/s reduction velocity.....	13
11. S-wave travel times vs. distance for deep ($z \geq 60$ km) and larger ($M_L(P) \geq 2.7$) seismic events shown with 4.7 km/s reduction velocity.	13
12. Top. S residuals after event relocation with polarization picks (red) and STA/LTA picks (blue) for shallow events.	
12. Bottom, zoomed-in for distances less than 1°	14
13. Wood-Anderson equivalent waveforms for 90 seconds of data from April 8, 2005, about 8 hours after an $M=6+$ earthquake in the Payang Basin.	15

14. Magnitude comparison.....	16
15. Left. $M_L(P)$ versus NEIC m_b , Global CMT and regional moment tensor (Baur, 2007) M_w .	
15. Right. Frequency-magnitude relation for 4,000+ events within 600 km of the array and at least 3 magnitude observations with minimum signal-to-noise ratio of 3 per event.....	16
16. Regional moment tensor solutions.....	17
17. Left. Comparison of NEIC (green circles) and automated Hi-CLIMB (blue squares) seismic event locations for the PXR reveals a general SW NEIC location bias that can reach more than 40 km (average value for 11 common events is 25 km).	
17. Right. Automatic (blue) and manual (orange) locations for 50 PXR events differ on average by less than 2 km and differences do not exceed 8 km.....	22
18. Map of the central PXR showing manual locations for 50 events.....	23
19. Map of 41 GT5 _{95%} candidate events (circles).	25

List of Tables

1. 143 regional moment tensor solutions in Nepal and southern Tibet	18
2. Manual locations of 41 GT5 _{95%} (candidate) events	26

1. SUMMARY

Broadband seismic data acquired during the Hi-CLIMB experiment are used to study seismic events and path propagation in the Nepal Himalaya and the south-central Tibetan Plateau. The 2002–2005 experiment consisted of 233 stations along a dense 800 km linear north-south array extending from the Himalayan foreland into the central Tibetan Plateau. The main array was flanked by a 350 km x 350 km sub-array in southern Tibet and central and eastern Nepal. The dataset provides an opportunity to obtain seismic event locations for ground truth evaluation, and to determine source parameters.

The Hi-CLIMB experiment revealed intense and distributed seismicity in the south-central Tibetan Plateau. The Hi-CLIMB seismic event database contains over 22,500 events from June 2004 to August 2005. Automated arrival time picks from vertical component data consist primarily of P waves and relatively few S waves. To increase the number of S picks and to obtain accurate picks at distances larger than 1° – 2° , we implemented an automatic S-wave picker that utilizes signal attributes from three-component seismic data. We adjusted picking parameters and thresholds to optimize automatic picks relative to manual picks from events distributed throughout south-central Tibet. For shallow events, Sg can be picked accurately to the Sg/Sn crossover distance of about 3° while Sn arrivals are absent. Deep events beneath the southern Tibetan Plateau and the High Himalayas produce clear S arrivals that can be picked to 5° – 6° distance. We applied the S-picker to 5790 $ML(P) \geq 2.0$ events resulting in about 93,000 high quality S picks.

We identified 54 GT5-candidate events with $ML(P) \geq 2.0$ of which 50 satisfy the GT5 criteria at the 95% confidence level. Waveform modeling resulted in 143 earthquake moment tensor solutions.

2. INTRODUCTION

The broadband dataset from the 2002–2005 Hi-CLIMB seismic array in the Himalayan-Tibetan collision zone is unique in its large aperture and dense station spacing. The purpose of our research was to improve source and path calibration in regions of poor crustal propagation to enhance capabilities to estimate magnitude and yield of seismic events in low Q and highly scattering environments. We have three linked objectives. The first is to obtain high-precision ground-truth seismic event hypocenters. The second is to provide seismic moment and independent depth estimates from waveform modeling of local and regional earthquakes. The third is to determine the distance evolution of seismic coda, utilizing the quasi-continuous control offered by the dense, laterally large network (paying emphasis on mantle coda), important for low Q areas.

3. THE HI-CLIMB DATASET

The Hi-CLIMB broadband seismic experiment (Nabelek, et al., 2005; 2009) consisted of 233 sites in Nepal and the south-central Tibetan Plateau (Figure 1). The network operated from 2002 through 2005 and each site was occupied for 12 to 20 months. The network consisted of an 800-km long north-south array covering the India-Eurasia collision zone from the Ganges foreland

across the High Himalayas into the Tibetan Plateau. Station spacing was 3-4 km in the south and about 8 km north of the Yarlung-Tsangpo suture. Complementary lateral deployments, with 30 to 40 km station spacing in central and eastern Nepal and southern Tibet significantly improve seismic event location capabilities, provide wave propagation control for the transition from the foreland into the plateau and allow high-resolution 3-D wave speed and attenuation tomography. The Hi-CLIMB data, recorded continuously at 40 and 50 sps, provide a unique opportunity to determine locations, source parameters and coda distance evolution of small sized seismic events at unprecedented accuracy in central Asia.

Figure 1 shows the large spatial extent and small station spacing of the Hi-CLIMB array. This study focuses on data from Phase 2 of the project (red symbols), in an area which is relatively less known compared to the Himalayan region in Nepal, for which regional network data are available.

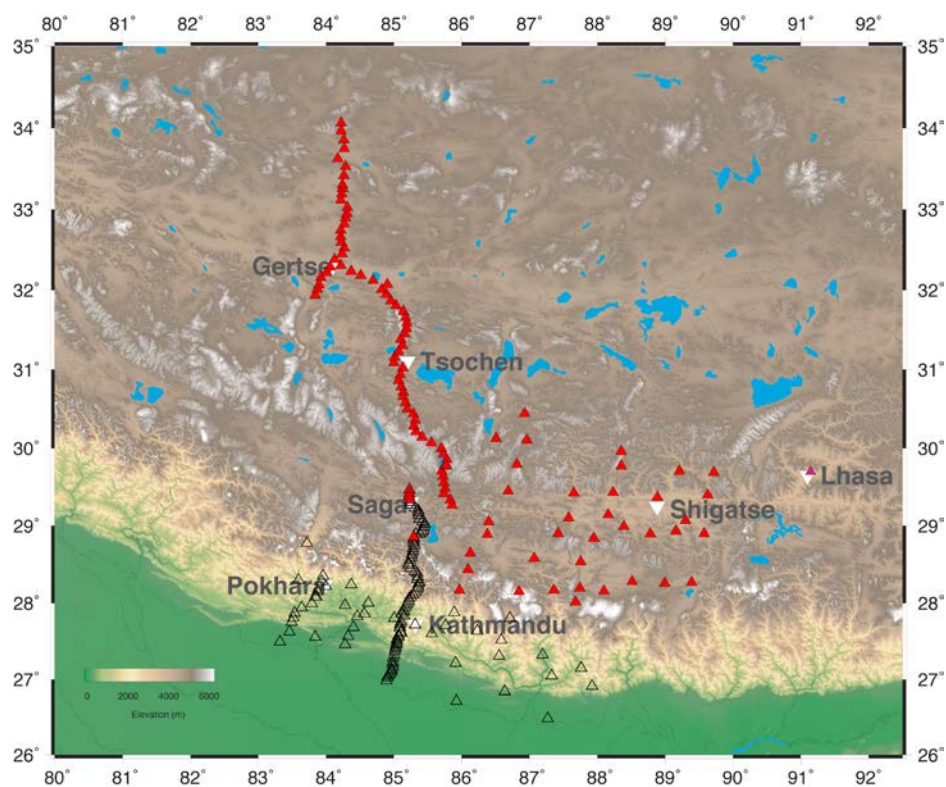


Figure 1. Map of the Hi-CLIMB seismic network (phase-2: red triangles, phase-1: open triangles) and permanent GSN station Lhasa. During the first 20 months of Hi-CLIMB (Nepal and South Tibet), 75 broadband instruments were available while during the second 15 months (South and Central Tibet), 111 instruments were available. Altogether, 233 sites were occupied.

4. SEISMIC EVENT LOCATION

4.1. Event Detection and Initial Location

The Hi-CLIMB waveform database (1.4 TB) has been organized using the Antelope software developed by Boulder Real Time Technologies (BRTT). The package includes modules for automatic detection and arrival time picking, event-arrival association, and event location. Initial analysis of event detections revealed about a thousand legitimate event detections per week (Figure 2). Using a low detection threshold (STA/LTA ratio of 3.0 in a frequency band of 2-10 Hz) and an association rule of 7 or more phases needed to constitute an event resulted in an initial database of almost 110,000 events for the 15-month June 2004 to August 2005 period. This corresponds to an average of 240 events per day and is more than 500 times the number of seismic events listed in the United States Geological Survey (USGS) Preliminary Determination of Epicenters (PDE) catalog for the same region and period. Many of these events are aftershocks of the 2004/193 M=6.2 earthquake on the west side of the array.

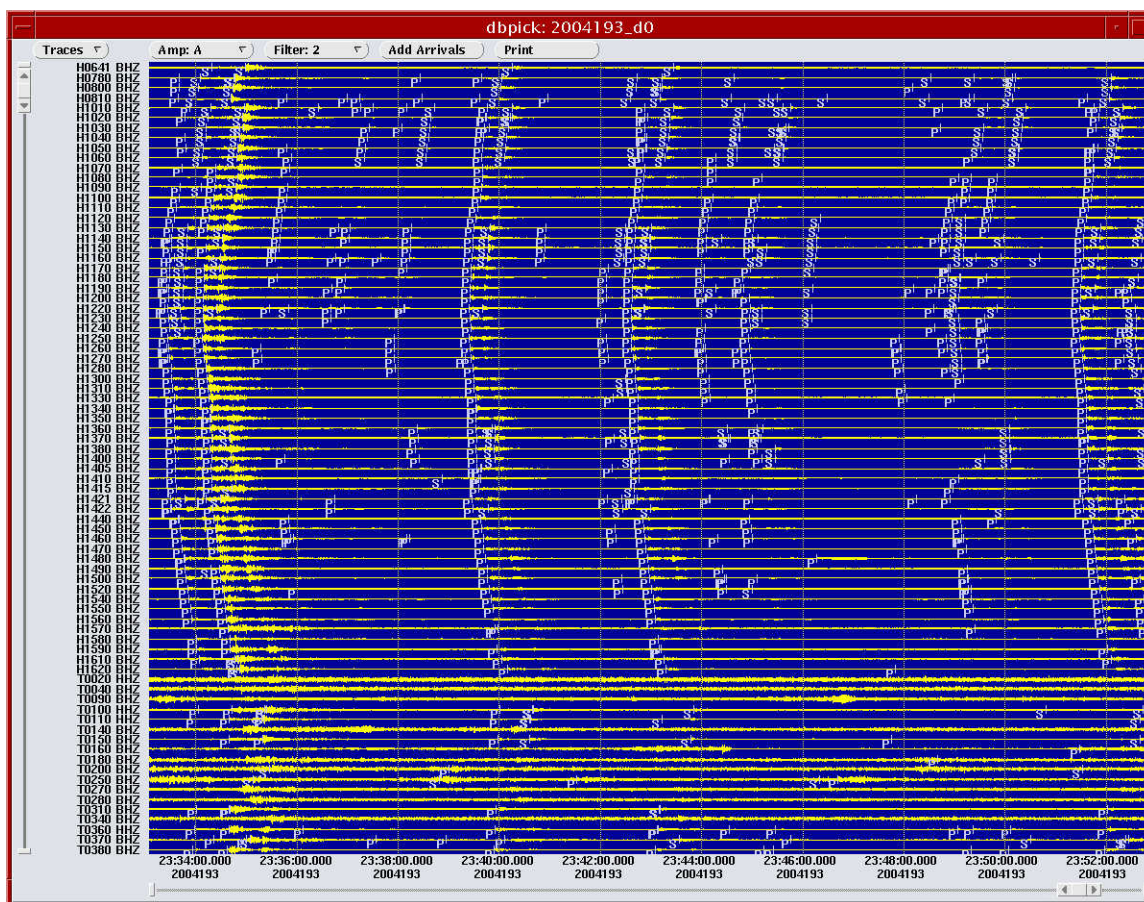


Figure 2. Event detection for a 20-minute Hi-CLIMB data window (Julian day 193, 2004, start at 23:33 UTC). *P- and S-phase association has been performed and four stronger local events were recorded across the array and many smaller events at specific station groups only.*

The large number of events rendered manual inspection unfeasible. We developed post-processing filters to remove spurious detections and erroneous phase and event associations to automate data management. Figure 3 shows a simplified flowchart of post-processing steps that implement simple logic considerations about what constitutes a valid seismic event. The main considerations are (1) stations close to each other have to record an event and (2) stations close to the epicenter have to record an event. The initial arrival set for a declared event could contain a significant number of wrongly associated detections resulting in a grossly incorrect location. Problems, for example, stemmed from wrong phase association caused by simultaneously occurring events in different locations within the Hi-CLIMB array region, misplaced seismicity from the great 2004 Sumatra earthquake sequence or incorrectly associating P arrivals as S arrivals, or vice versa. The initial filter eliminates spurious detections or entire events based on (1). In later stages, we expect locations to be basically correct and thus require (2).

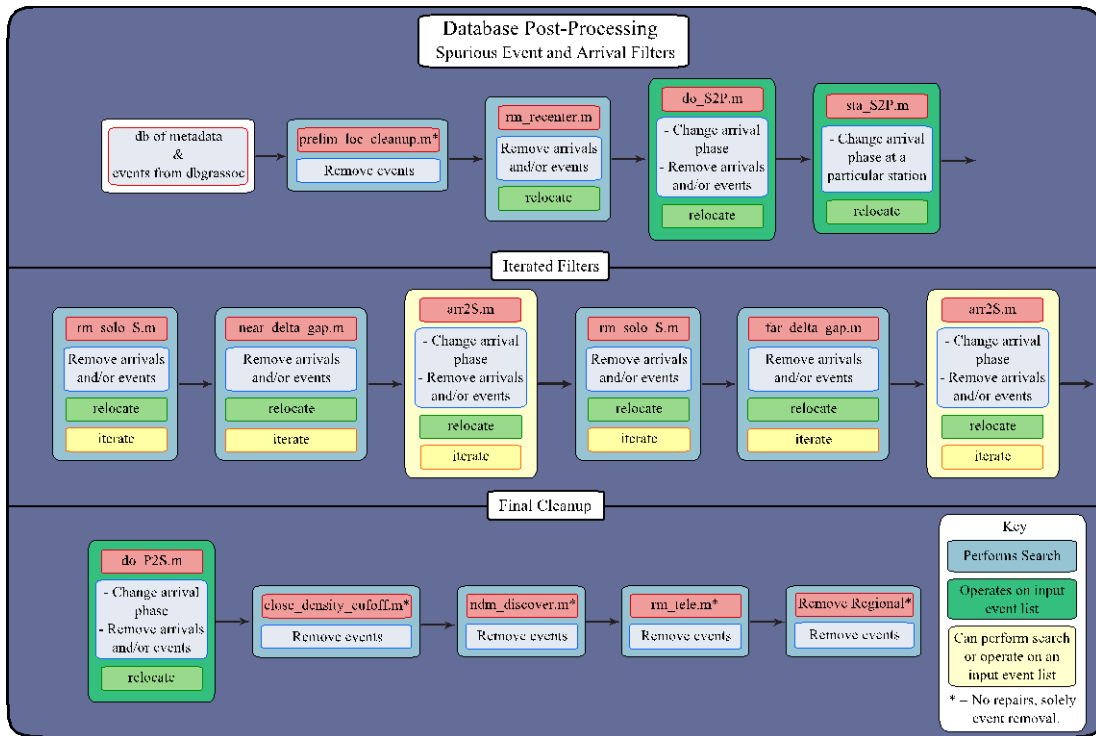


Figure 3. Simplified flowchart of database post-processing steps performed to clean up the initial associated event table. Processing steps fall into two groups: (1) removing or reassigning phase picks to obtain a more consistent set of phase picks for an event leading to improved location after a relocation (green box) or (2) removing spurious events for which the set of phase picks could not be fixed (blue box “Remove events”). Details are described in Carpenter, 2010.

We manually picked P- and S-arrivals to refine the 1D velocity model for location and to evaluate automatic pick quality. We used two events from the Pumqu-Xianza Rift (PXR) with clear P and S onsets across the Hi-CLIMB array to refine the model because their hypocenters are well constrained and event-station paths sample southern Tibet resulting in a representative 1D model. Figure 4 shows the observed and predicted (tib3p) travel times for the refined (tib3p) 1D model. The observed P arrivals are consistent with a simple two-crustal-layer over mantle

model; the shallow low-velocity layer agrees with receiver function analysis (Nabelek, et al., 2009) and waveform modeling (Baur, 2007). A single crustal S-velocity layer is required by the traveltime data (Figure 4) since S_n crossover distance is beyond the P_n crossover distance (at about 300 km). The upper mantle velocities in tib3p are based on the arrival times from the additional near-Moho events from the south. The model tib3p, which we uniformly used for locating the events, is strictly applicable only for the Lhasa block. South of the Yarlung-Tsangpo suture and north of the Bangong suture the velocity structure is clearly different, particularly the depth of Moho.

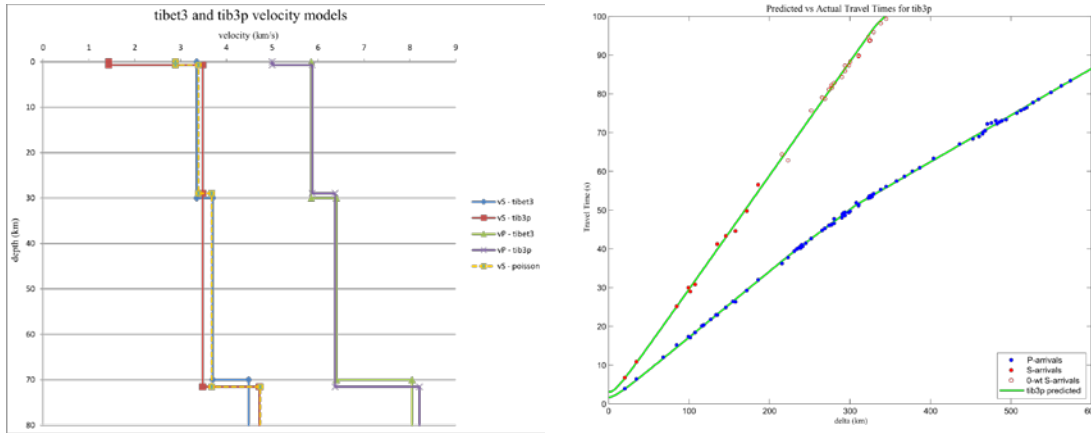


Figure 4. Right. Observed (dots) and predicted (green lines) travel times vs. distance from the epicenter for a manually picked PXR event.

Figure 4. Left. Refined velocity model tib3p based on these observations was used for final location of the Hi-CLIMB dataset. Earlier analyses used model tibet3, which was estimated from several type events within study region. Red open circles are analyst-picked S-arrivals.

To assess the quality of the automatic arrival-time picks and to evaluate whether a single 1D model suffices for our location purposes, we manually picked P- and S-arrivals for 16 stronger events distributed throughout the study region. Figure 5 shows differences between manual and automatic picks for P and S arrivals. At distances less than 300 km for P wave and less than 100 km for S waves the automatic picks generally agree with the manual picks; at greater distances the automatic picks are generally late. We used this information to construct a distance weighting scheme giving full weight for P waves from 0° to 2° distance with a linearly decreasing weight out to 8° . For S waves, full weight was given up to 1° with a linear decrease to zero weight at 2° . However, event locations were not very sensitive to changes in the velocity model or the weighting. Locations based on manual and on automatic picks are also very similar. For the 16 manually picked events, the mean epicenter difference is less than 3 km and for a set of 50 $2.1 \leq M_L \leq 4.8$ events in the PXR (Monigle, et al., 2012), we found a median difference of less than 2 km with a maximum difference of less than 8 km (see section 6.1). The largest discrepancies occurred for events prior to the completion of the entire array.

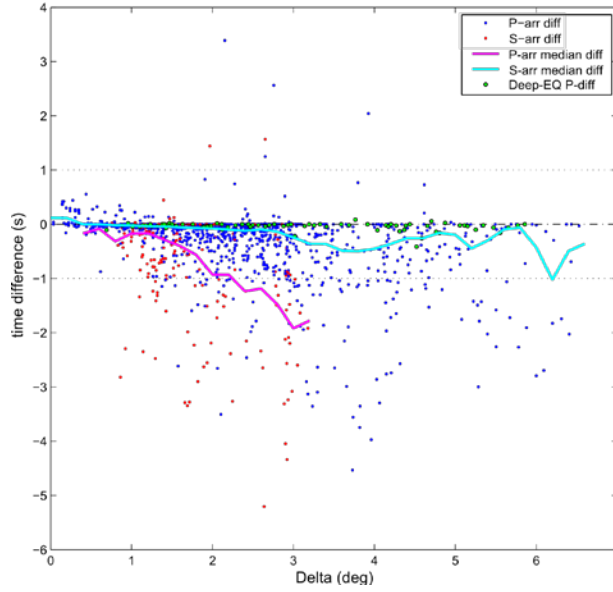


Figure 5. Differences between manually and automatically picked arrival times for 16 stronger regional events. *P*-differences in blue, *S*-differences in red, medians are solid lines (*P*: cyan, *S*: magenta). Note the small differences for a deep event (with impulsive *P*-onset) for all observed distances. Based on these observations, we use *S* arrivals for event location only from 0 to 1.5 degrees. Similarly, we downweight *P* waves arrivals from epicentral distances greater than 3 degrees.

The final seismic event database of over 22,500 events (about 50 events per day) passing all location quality tests includes over 7,900 events (Figure 6) with at least 25 *P* and *S* arrivals, corresponding to well-located events throughout the map area. Of these, 4,500 have a local magnitude $M_L(P) \geq 2.0$. The locations based on automatic arrival time picks utilize *S*-arrivals, constraining the epicenters, and correlate with geologic structures seen in satellite imagery suggesting they are quite accurate; for some events the USGS PDE locations show a mismatch of up to 50 km (see section 6.1 for quantitative analysis of PDE and automatic location bias in the PXR). Seismicity is distributed throughout the study area. Most shallow seismicity north of the Yarlung-Tsangpo Suture (YTS), i.e., north of 29.5° , is in an area not investigated by previous experiments. The most active source regions are north-south trending grabens in the Lhasa terrane. We located almost 10,000 events in the Payang Basin (near $30^\circ\text{--}31^\circ\text{N}$, 84°E) following two $M_w > 6$ main shocks in July 2004 and April 2005, respectively. The distance from the Payang Basin to the closest stations is more than 100 km precluding consideration for GT-level locations (in addition to a one-sided station distribution). However, our locations for the two main shocks are consistent with the InSAR-derived fault area (Elliot, et al., 2010). Vigorous seismicity (1,300+ events) was also observed from the vicinity of the PXR ($\sim 30^\circ\text{N}$, 88°E). There, due to close-by stations, differences between automatic and manual locations are only a few kilometers (see section 6.1). Comparison with InSAR and manual locations suggests that epicenter uncertainties for most events in Figure 6 are probably less than 10 km.

Adding requirements of distance to closest station $D_{\min} \leq 50$ km, azimuthal gap $Az \leq 225^\circ$, and $M_L(P) \geq 2.0$ results in a high-quality subset of about 600 seismic events. In addition to tighter clustering, event depths are well resolved: events north of the southern Lhasa Block are generally

shallow ($<20\text{km}$) while events south of it are either shallow or close to the Moho (Figure 6) as observed in previous studies (e.g., Langin, et al., 2003; Monsalve, et al., 2006; Liang, et al., 2008). Events close to the Moho propagate across the entire array with mantle velocities and therefore their depth estimates are completely governed by the Moho depth. In tib3p the Moho is at 71 km depth but in reality it decreases south of the Yarlung-Tsangpo Suture to about 50 km under the Himalayas (Nabelek, et al., 2009). The depths of the deep events can be simply shifted to the appropriate hypocenter depth without altering the travel time fit by choosing the

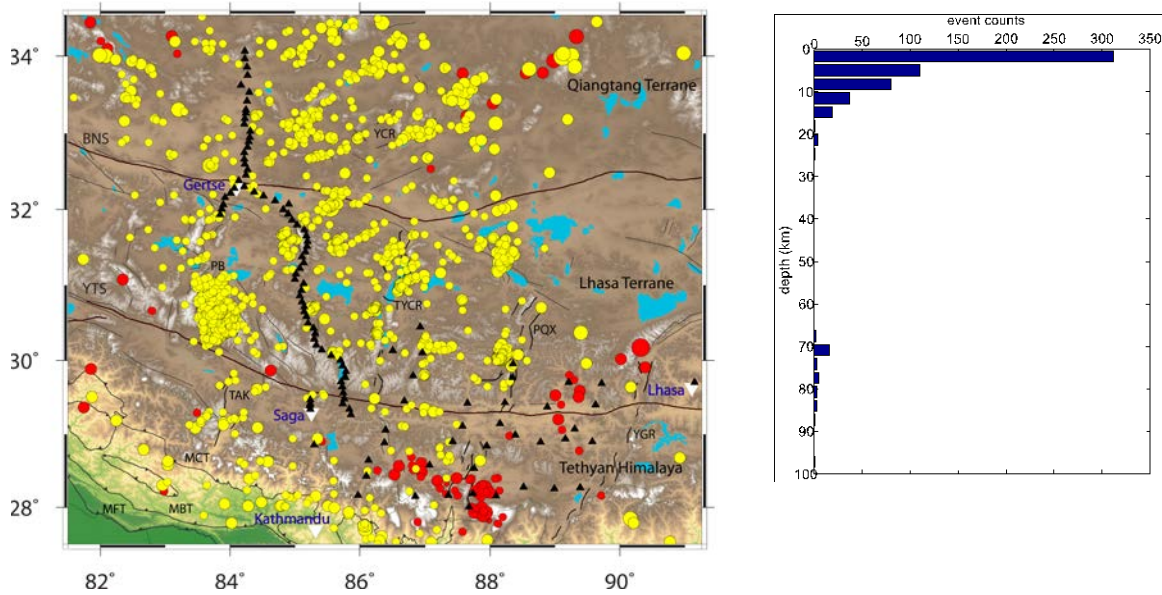


Figure 6. Left. Map of 7,900+ events with at least 25 P and S picks shows high-quality locations with distinct clustering. *Colors distinguish crustal (yellow) from near-Moho events (red; $z \geq 65\text{km}$). Black triangles are June 2004 to August 2005 stations. PB is Payang Basin, PQX Pumqu-Xianza Rift, and YTS Yarlung-Tsangpo Suture. Red events outside network, e.g. in the Qiangtang terrane, have poorly determined depth. The numerous shallow events north of the Yarlung-Tsangpo suture ($>29^\circ\text{N}$) have not been covered by previous experiments.* **Figure 6. Right.** Requiring $D_{\min} \leq 50\text{ km}$, $\text{gap} \leq 225^\circ$, and $M_L \geq 2.0$ results in ~ 600 events with well-constrained depth. *The depth distribution is bimodal as observed previously; deep events are observed beneath the Tethyan Himalaya (mainly between $\sim 86-88^\circ\text{E}$) and near the Yadong-Gulu Rift.*

4.2. Polarization S-Picker

We used the Antelope software for automatic detection and arrival time picking and for event association and location. The arrival picks were obtained through STA/LTA analysis on vertical component seismic data. Our arrival time database does contain a significant number of S-wave picks. However, due to picking from vertical components, the quality of the S picks overall is relatively low and degrades rapidly with epicenter distance (Figure 5) forcing us to use S arrivals for location only to 2° epicenter distance. While a few accurate S picks from close-by stations generally suffice to constrain seismic event locations, additional accurate S picks are important

for 3D S-wave velocity inversions. Combined P- and S-wave tomography provides critical information regarding composition and physical state of the crust and upper mantle.

We implemented a new automatic, polarization-based, S-wave picker to increase the number of S picks and to obtain accurate picks at distances larger than 1° - 2° . The S picker uses signal attributes from three-component seismograms to determine the S-wave onset from shear wave energy and polarization analysis. The picker has been adapted from an implementation by Diehl, et al., 2009 with polarization analysis following Cichowicz, 1993. First we rotate the ZNE data into the LQT ray-coordinate system to separate P-wave (L-component) from S-wave energy; the T-component includes SH and the Q-component SV energy, respectively. For rotation, we used the ‘known’ event location and velocity model, since the events had already been identified and located with picks, primarily P phases, from the Antelope STA/LTA algorithm. The traces are then filtered using a Wood-Anderson and a 0.5 Hz high pass filter. The Wood-Anderson filter integrates the velocity signal to displacement, essentially acting as a low-pass filter.

An S phase is picked when rectilinearity, directivity relative to the incoming P wave, as well as ratio of transverse to overall energy and the transverse amplitude reach a data-dependent threshold within a short, user-defined time window. Rectilinearity $R(t)$ is defined as the degree of linear polarization of the incoming particle motion (e.g., Cichowicz, 1993; Diehl, et al., 2009); $R(t)$ is one for body waves. Directivity $D(t)$, which represents the angle between the longitudinal (L) direction and the eigenvector associated with the maximum eigenvalue (see, e.g., Cichowicz, 1993), is zero for P and one for S waves. The energy ratio $H(t)$ is the S-wave energy (sum of squared amplitudes) relative to total energy and is maximum for S arrivals. The weight function $W(t)$ is simply the square of the ratio of the maximum amplitude on either the T or Q component within a short picking interval relative to the overall maximum amplitude on either component within the S-wave picking window (see below); we use the squared amplitude to accentuate the S wave arrival (cf. Diehl, et al. 2009). $W(t)$ reaches its maximum W_{\max} when the picking interval includes the overall maximum amplitude. We combine the polarization, $R(t)$ and $D(t)$, and amplitude, $H(t)$ and $W(t)$, attributes in a characteristic function $CF(t)$:

$$CF(t) = R^2(t) * D^2(t) * H^2(t) * W(t) \quad (1)$$

$CF(t)$ is near zero for incoming P wave energy and near one for incoming S wave energy. The procedure is illustrated in Figure 7 and variables and their values are explained in Table 1. The three traces in Figure 7a show the LQT-rotated seismograms including the P-phase pick and the predicted (gray) S-phase arrival *Spre*. The predicted arrival time is for the initial ‘known’ event location and the *tib3p* velocity model (Figure 4). Figure 7b shows the characteristic function $CF(t)$ and the time window from *SW1* to *SW2* within which the S pick has to occur; the window is centered on the predicted S-arrival time and its length depends on epicenter distance. The second trace shows the weight function $W(t)$.

A coarse pick at time *WS* (orange vertical line in Figure 7b) is obtained when the weight function $W(t)$ (blue line) exceeds a threshold *tr1* (thin red line) determined from the mean and standard deviation of the weight function $W(t)$ in the window *W1* to *W2*. The window end, *W2*, coincides with the earliest possible S-arrival time, *SW1*, and the window start *W1* is at the midpoint between the P arrival and *W2*. This window is chosen to exclude direct P energy, to precede the S arrival, and to be long enough to characterize the T and Q component ‘background’ level. The threshold *tr1* is set sufficiently higher than the measured noise level so that the coarse pick *WS* clearly identifies the S energy. (In this example, the ‘background’ level

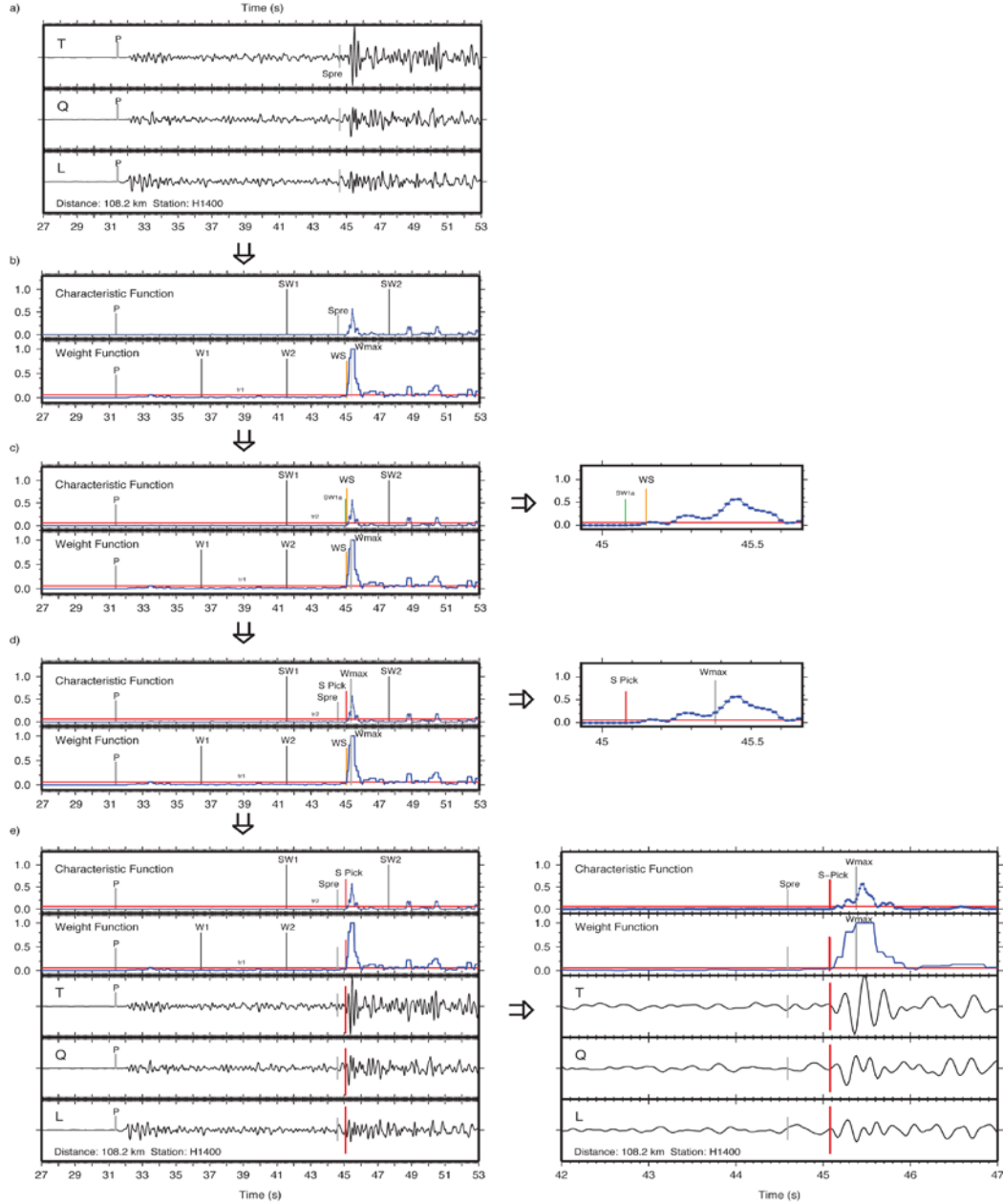


Figure 7. Step-by-step process for S picking by polarization method for station H1400, 108 km from the 3 July 2005 $M_L(P)=3.0$ earthquake at 31.55°N and 85.62°E . For details of the picking process refer to text. A) Rotated L, Q, T components with predicted S arrival Spre. B) Characteristic function CF(t) and weighting function W(t) built from the seismic traces. SW1 and SW2 define picking window around Spre. Threshold tr1 is calculated between W1 and W2; WS marks where W(t) crossed tr1. Wmax is the maximum amplitude of W(t). C) WS is projected on CF(t). SW1a is the first minimum of CF(t) prior to WS and the threshold tr2 (red line) is built between SW1 and SW1a. Zoomed-in CF(t) trace to right. D) Wmax is projected on CF(t). The final S pick is the first non-local minimum below the threshold tr2 on CF(t) prior to Wmax. Zoomed-in CF(t) trace to right. E) Final S pick (red) on seismic traces, zoomed-in on right.

of $W(t)$ is very low and therefore $tr1$ is also appears quite low). We expect the actual S arrival to closely precede WS . If WS cannot be found for the given $tr1$, no pick is attempted, thus eliminating data with low signal-to-noise ratio.

For the final pick, we use the *characteristic function* $CF(t)$, which incorporates S wave signal strength attributes, $H(t)$ and $W(t)$, as well as polarization attributes, $R(t)$, $D(t)$ and $H(t)$. For a pick (Figure 7c), $CF(t)$ (blue) has to exceed a threshold $tr2$ (red horizontal line), defined from mean and standard deviation of $CF(t)$ between times $SW1$ and $SW1a$, which is the first minimum of $CF(t)$ prior to WS . To avoid spurious maxima in $CF(t)$ prior to the S arrival, the algorithm works backwards in time along $CF(t)$ starting at $Wmax$. A pick is declared when $CF(t)$ reaches a minimum after it has dropped below the threshold $tr2$, i.e., before $CF(t)$ reaches the threshold, and stays below the threshold. The example shown in Figure 8 shows a case where $CF(t)$ had reached a local minimum. To avoid local minima, the algorithm, for several samples, continues its search backwards in time to be able to ‘climb’ over preceding maxima and to find the instance where $CF(t)$ reaches a minimum after dropping below the threshold $tr2$ and stays below it.

Figure 8 shows additional examples of S picks as a function of epicenter distance, from 65 to 255 km, for the upper-crustal event of Figure 7. All arrivals are crustal S_g phases considering the 70 km thick crust of the Lhasa block. The picks are very good. For this event, we obtained 34 S-phase picks with the polarization S picker compared with 5 S picks from Antelope STA/LTA analysis. Figure 9 compares polarization picks to STA/LTA based picks for different distances for another crustal seismic event. For the set of common stations, the STA/LTA picks are 0.7 s later than our new S picks. It is no surprise that STA/LTA based picks are late considering the higher noise level in the P coda that precedes the actual S arrival; however in some cases the STA/LTA picks can also be early.

We have adjusted the picking parameters and thresholds multiple times to optimize automatic picking results for our data based on visual inspection of the algorithm’s performance and on comparison with manual picks from events distributed throughout south-central Tibet (see below). No pick is declared when the thresholds for $W(t)$ or $CF(t)$ are large or when $CF(t)$ oscillates around its threshold.

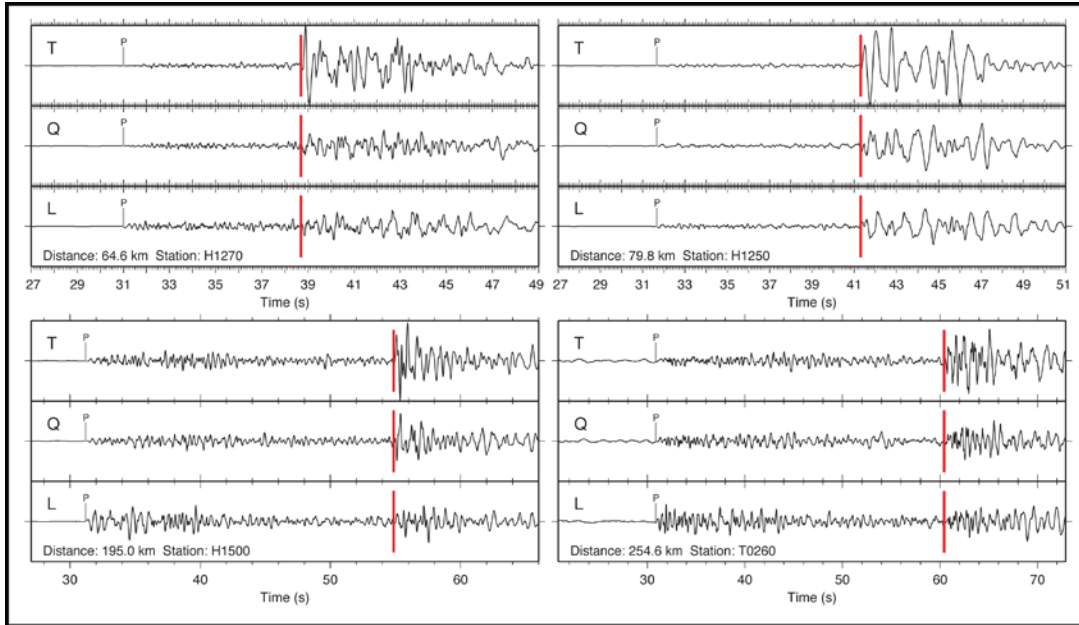


Figure 8. Examples of S-phase picks with increasing distance, from 65 to 255 km, for same event as in Figure 7. Red are automatic S picks using the new picker.

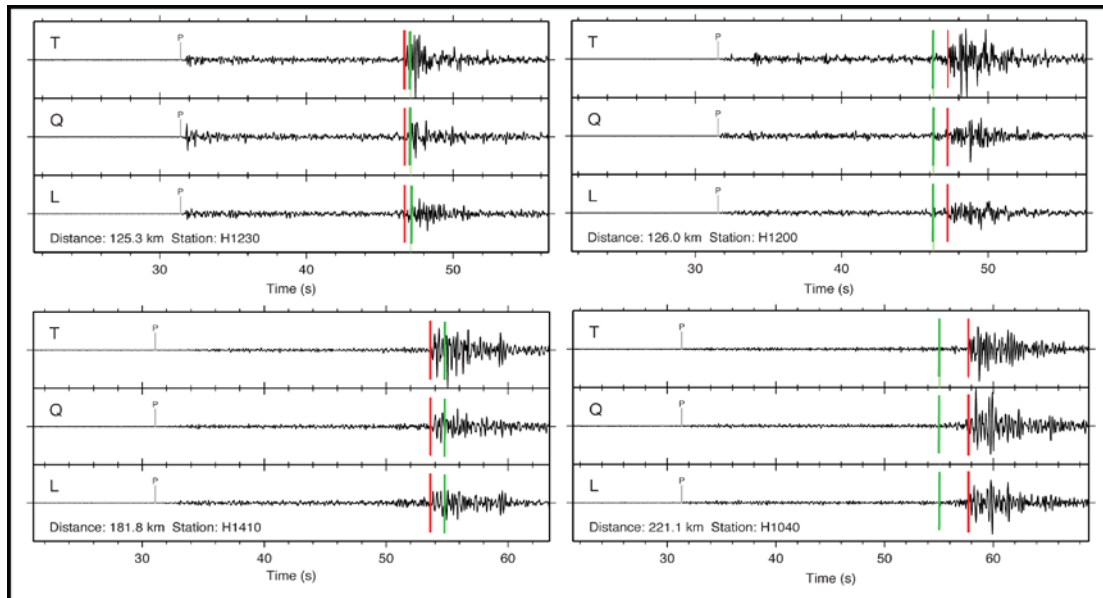


Figure 9. Polarization (red) vs. STA/LTA (green) S picks for the 15 July 2004 $M_L(P)=2.9$ earthquake (30.66°N , 83.83°E). On average STA/LTA S picks are 0.7 s late, although the STA/LTA picks can also occur before the polarization S pick (and the actual arrival). Because the STA/LTA picks were made with P-waves as the primary target (vertical component and higher (2-10 Hz) frequency band), their substantially poorer performance is not surprising.

The polarization S picker led to a significant increase in the number of successful S picks and improved the pick precision compared to STA/LTA method.. For example, for the PXR dataset of 50 high-quality events (Monigle, et al., 2012), the STA/LTA picker had found 478 S arrivals, while the polarization picker found 1147. Even more important, at shorter distances, where pick quality is high, the number of S picks almost doubled from 115 to 206. The significant difference at short distances (≤ 100 km) is critical for accurate hypocenter locations; there the polarization picker detected many more S arrivals and, on average, the polarization and manual arrival times are identical.

Next, we applied the polarization S picker to 5,790 $M_L(P) \geq 2.0$ events within 2° from the closest station and with at least 15 picks (P and S combined) in our original database. These events already have well-constrained epicenter locations with well-recorded signals across a significant part of the Hi-CLIMB array. We do not expect their locations to change much when changing and adding S picks. For the 5352 shallow events ($z \leq 30$ km), S_g can be picked reliably to the S_g/S_n crossover distance of about 3° while S_n arrivals are either absent or too weak to be picked reliably. In contrast, the 222 deep events ($z > 60$ km) beneath the southern Tibetan Plateau and the High Himalayas produce clear S arrivals that can be picked to 6° - 7° distance, crucial to constrain the uppermost mantle S-wave velocity structure beneath southern Tibet. We obtained about 93,000 S picks almost doubling the number of picks compared to STA/LTA-based picks and, at short distances of $\Delta < 1^\circ$, more than tripled the number to about 6,500 S picks.

Reduced travel time plots for shallow and deep events (Figure 10 and 11) show a decrease in outliers and false detections for the polarization S picks. For shallow events, S arrivals are generally consistent with an average crustal velocity of 3.5 km/s; however, as the waveform examples show, the arrival time spread is real and likely due to velocity variations in the shallow crust. For deep events, S_n arrivals are present out to about 7° and show a mantle S velocity of about 4.7 km/s. Large S_n arrival errors present beyond 4 degrees from the STA/LTA analysis were eliminated through the polarization picking process.

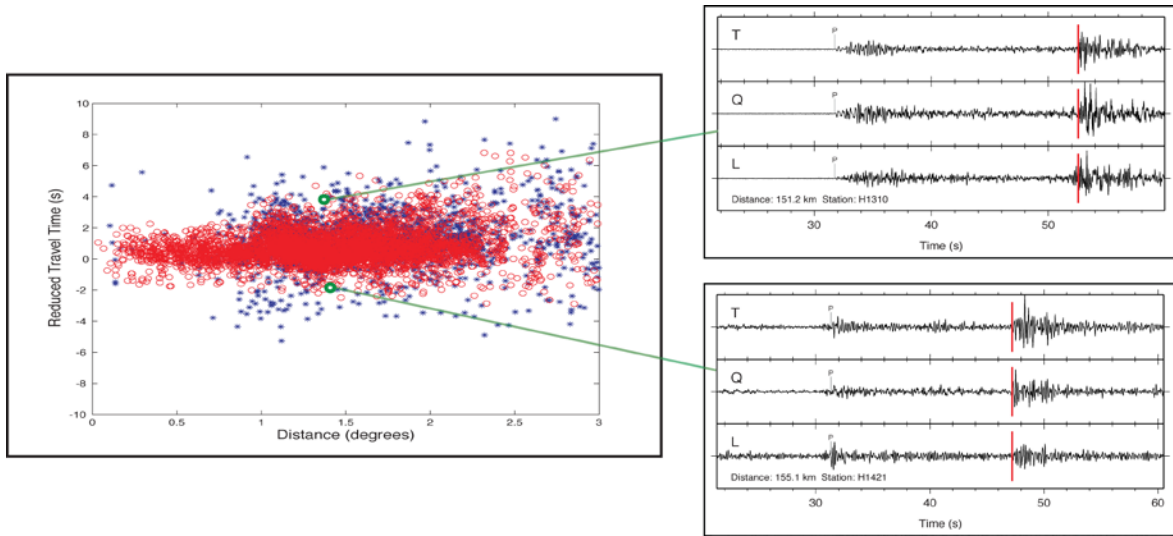


Figure 10. S-wave travel times vs. distance for small ($2.0 \leq M_L(P) \leq 2.7$) seismic events shown with 3.5 km/s reduction velocity. *Polarization picks (red) on top of STA/LTA picks (blue).* Note increased number of picks and reduction of outliers and false detections with polarization picker. Seismograms show spread in arrival times is real indicative 3D S-wave velocity structure.

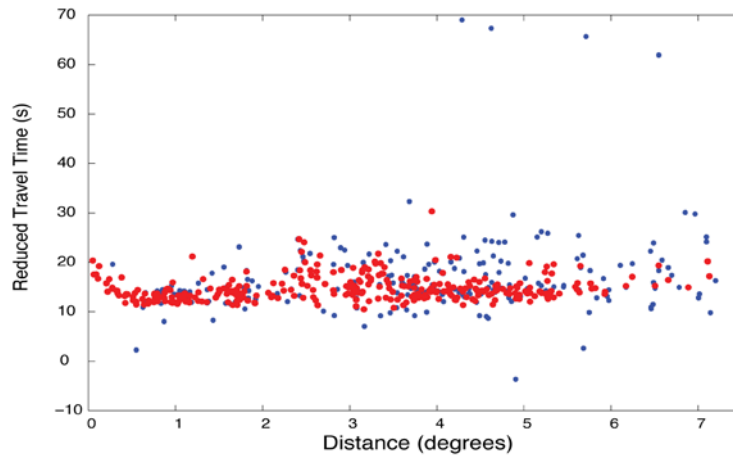


Figure 11. S-wave travel times vs. distance for deep ($z \geq 60$ km) and larger ($M_L(P) \geq 2.7$) seismic events shown with 4.7 km/s reduction velocity. *Polarization picks (red) on top of STA/LTA picks (blue).* Mantle S can be picked consistently to 6° - 7° distance with the polarization picker. Again we observe reduction of outliers and false detections with polarization picker.

We relocated the 5790 seismic events with the new polarization S picks. As expected for events with many phase picks, locations remained largely unaffected (average horizontal shift is 1.1 km) except for events at the periphery of the network; these moved slightly towards the network. Depth, on average, changed by less than one km even though more S picks were available per event. This is likely due to a combination of station coverage and number of pre-existing P arrivals, which yielded accurate initial hypocenters. In summary, out of 5790 events

only 156 changed depth by ± 5 km or more. Horizontally, only 85 events changed location by 0.1 degrees or more. For shallow events only 1.5% (88 out of 5352) changed depth by ± 5 km or more. For events at 60 km depth or deeper 14.4% (32 out of 222) changed depth by ± 5 km or more.

To further evaluate picking quality we compare relocation residuals for polarization and STA/LTA arrivals (Figure 12). For shallow events, average residuals were -0.07 s for polarization picks and -0.95 s for STA/LTA picks. For mid-range distances, 1° - 2.5° , the average STA/LTA arrival residual is negative (arrivals are consistently picked late). The polarization picks, however, are centered on a residual value of zero. The most striking difference is at close distances ($\leq 1^\circ$), where the number of arrivals increased while the residual spread decreased.

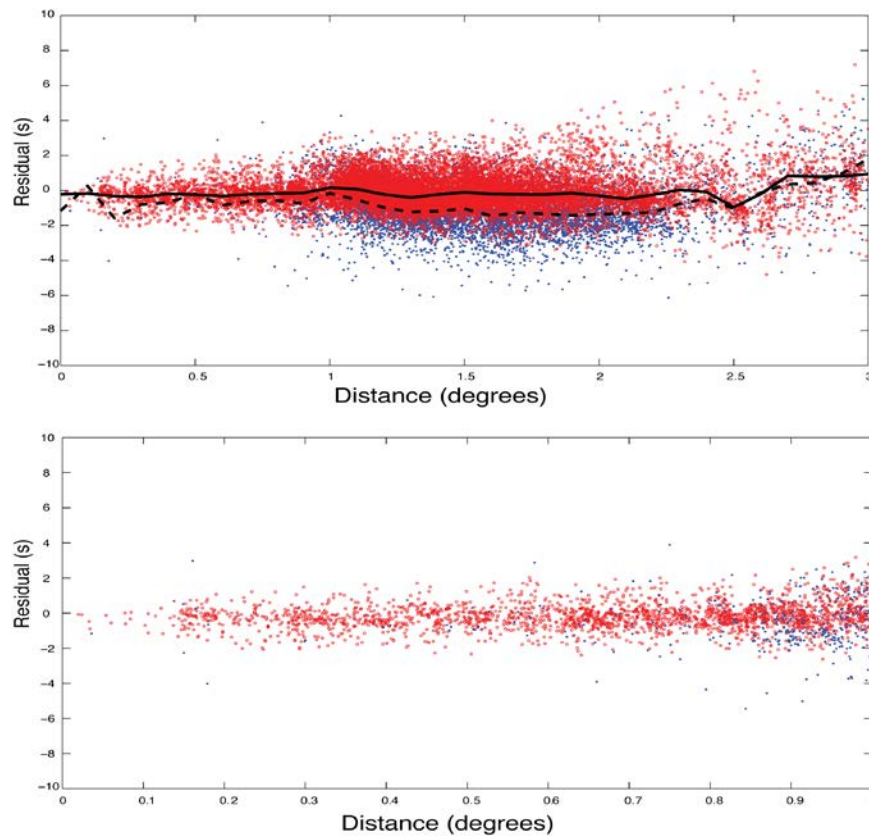


Figure 12. Top. S residuals after event relocation with polarization picks (red) and STA/LTA picks (blue) for shallow events. Solid and dashed lines are moving window averages for polarization and STA/LTA picks respectively. STA/LTA picks are consistently negative, meaning picks are late.

Figure 12. Bottom, zoomed-in for distances less than 1° .

4.3. $M_L(P)$

We used the Antelope module dbml to calculate local magnitude (M_L) from the vertical component seismograms for all events in the database with epicenter-station distances of 600 km or less. Usually M_L is determined from the maximum amplitudes on Wood-Anderson-equivalent horizontal seismograms with the maximum amplitude corresponding to an S-phase. We thus

originally defined the time window to be 1.5 times the S-P-time for a given station-event distance to obtain the amplitudes. However, during times of vigorous seismicity, we often encountered contamination by arrivals from closely following, larger events (Figure 13). Another complication arises from using vertical component data that underestimates S arrival amplitude, which led to systematically underestimated magnitudes.

To avoid both problems, we decided to estimate event size from a short time window containing only P waves (0.25 S-P-time, Figure 13). This approach eliminated contamination and provided a much cleaner magnitude dataset. Using the average theoretically expected S-to-P amplitude ratio of $(v_p/v_s)^3 \approx 5$ for earthquakes with a double-couple mechanism provides a physics-based approach to convert to S-based magnitude by simply adding a constant value of 0.7. We call this (corrected) magnitude $M_L(P)$ and use it consistently throughout this report.

On average, $M_L(P)$ is consistent with moment magnitude M_w from regional moment tensors (Baur, 2007) and matches teleseismic Global CMT M_w and USGS NEIC body wave magnitude m_b (Figure 14).

Our event $M_L(P)$ are medians based on at least 3 observations within 600 km distance and a minimum signal-to-noise ratio of 3 after Wood-Anderson filtering resulting in over 4,000 events with $M_L(P)$. The frequency-magnitude plot suggests completeness for $M_L(P) \geq 3.3$ within 600 km and $M_L(P) \geq 2.0$ within 150 km of the array (Figure 15).

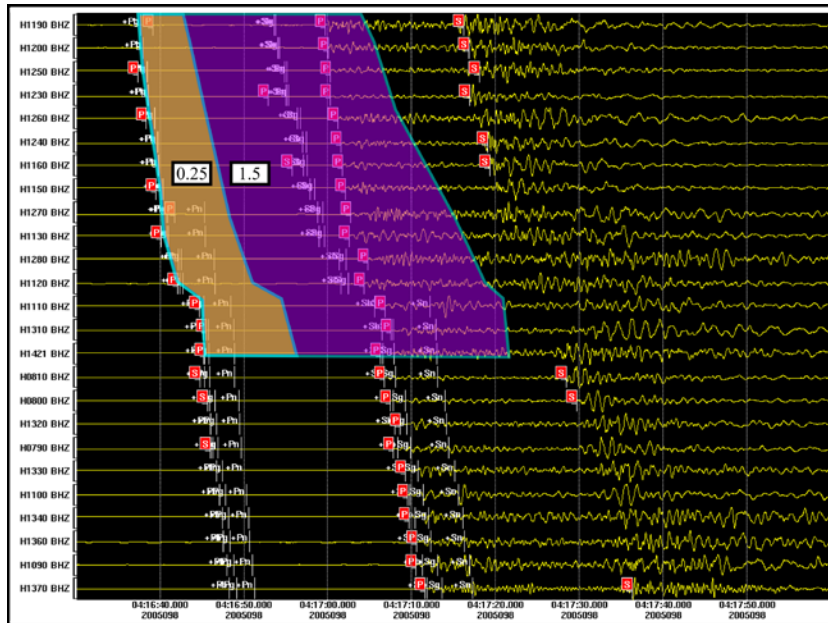


Figure 13. Wood-Anderson equivalent waveforms for 90 seconds of data from April 8, 2005, about 8 hours after an $M=6+$ earthquake in the Payang Basin. *A small event (first set of arrivals) is followed by a much stronger event (second set of P arrivals) within 1.5 times its S-P-time (purple area). The M_L for the first event based on the long time window is about 2 magnitude units too large. Another problem, apparent for the second event, is that vertical seismograms underestimate the amplitude of S-phases, which are predominantly recorded on horizontal components; in this case the S-to-P amplitude ratio is about 2 compared to the expected value of ~ 5 . We decided to determine magnitudes from a short window containing only the P arrival (0.25 S-P-time shown in brown).*

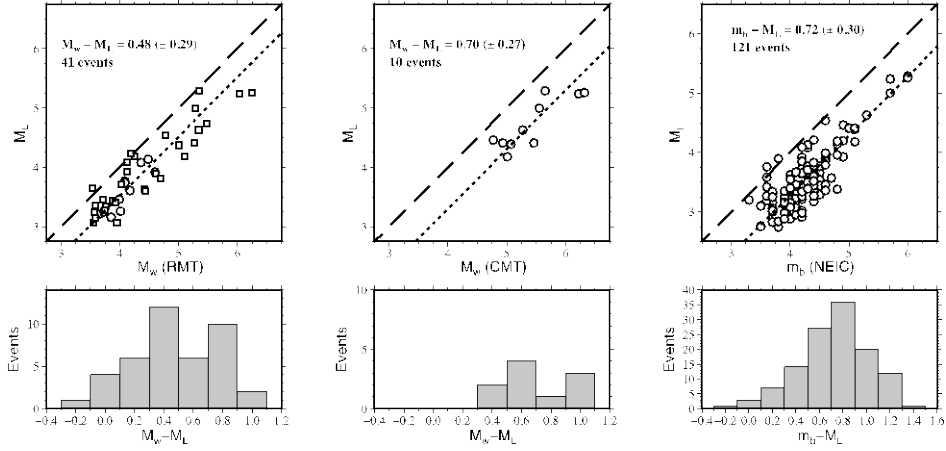


Figure 14. Magnitude comparison. M_L is local magnitude from P wave amplitudes. M_w (RMT), M_w (CMT), m_b (NEIC) are moment magnitude from regional moment tensor inversion, Global CMT analysis, and USGS NEIC body wave magnitude, respectively. Shown are common events. The average underestimation of uncorrected M_L of 0.5, 0.7, and 0.7, respectively, is consistent with the expected theoretical bias due the use of P instead of S waves. The scatter around the average (short dashes, long dashes correspond to one-to-one correspondence) is similar to scatter observed when regressing other magnitudes relative to each other (e.g., Braunmiller, et al., 2005).

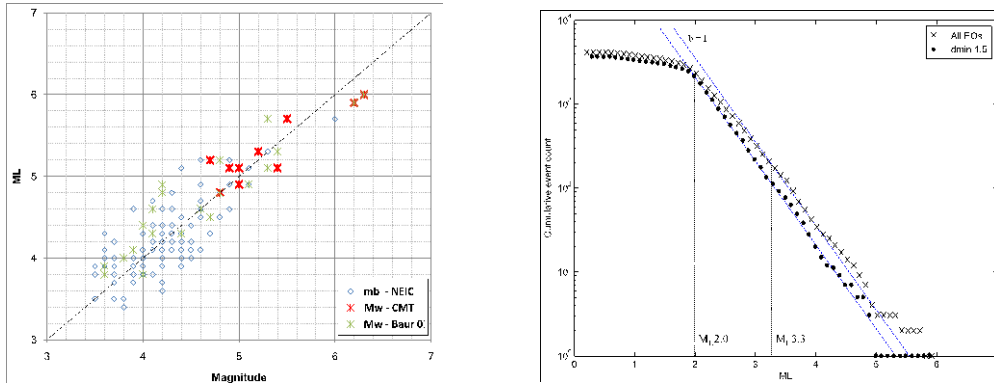


Figure 15. Left. M_L (P) versus NEIC m_b , Global CMT and regional moment tensor (Baur, 2007) M_w .

Figure 15. Right. Frequency-magnitude relation for 4,000+ events within 600 km of the array and at least 3 magnitude observations with minimum signal-to-noise ratio of 3 per event.

5. SOURCE PARAMETERS FROM REGIONAL MOMENT TENSORS

Regional moment tensor analyses was performed (Burtin, 2005; Burtin, et al., 2005; Baur, 2007; Monigle, et al., 2012) for 143 selected larger earthquakes in the Himalayan-Tibetan region using the full waveform inversion code developed by Nabelek and Xia, 1995. Results are

summarized in Figure 16 and listed in Table 1. Our efforts substantially expand the region's moment tensor catalog; our database includes most events analyzed by de la Torre, et al., 2007.

Burtin, 2005 tested analysis feasibility with permanent far-regional stations. Deriving station specific velocity models, he analyzed 27 $M_w \geq 4.5$ events that occurred from 1988 to 2001 within 1000 km of the closest station LSA (Lhasa, Figure 1) and along the southern boundary of the Tibetan Plateau. Long paths require analysis at long periods ($T \geq 33$ s), which limits parameter resolution and sets a high analysis threshold. For seismic events during 1991-1992, he also used data from the temporary Pascal 91-92 deployment (e.g., Zhu and Helmberger, 1996).

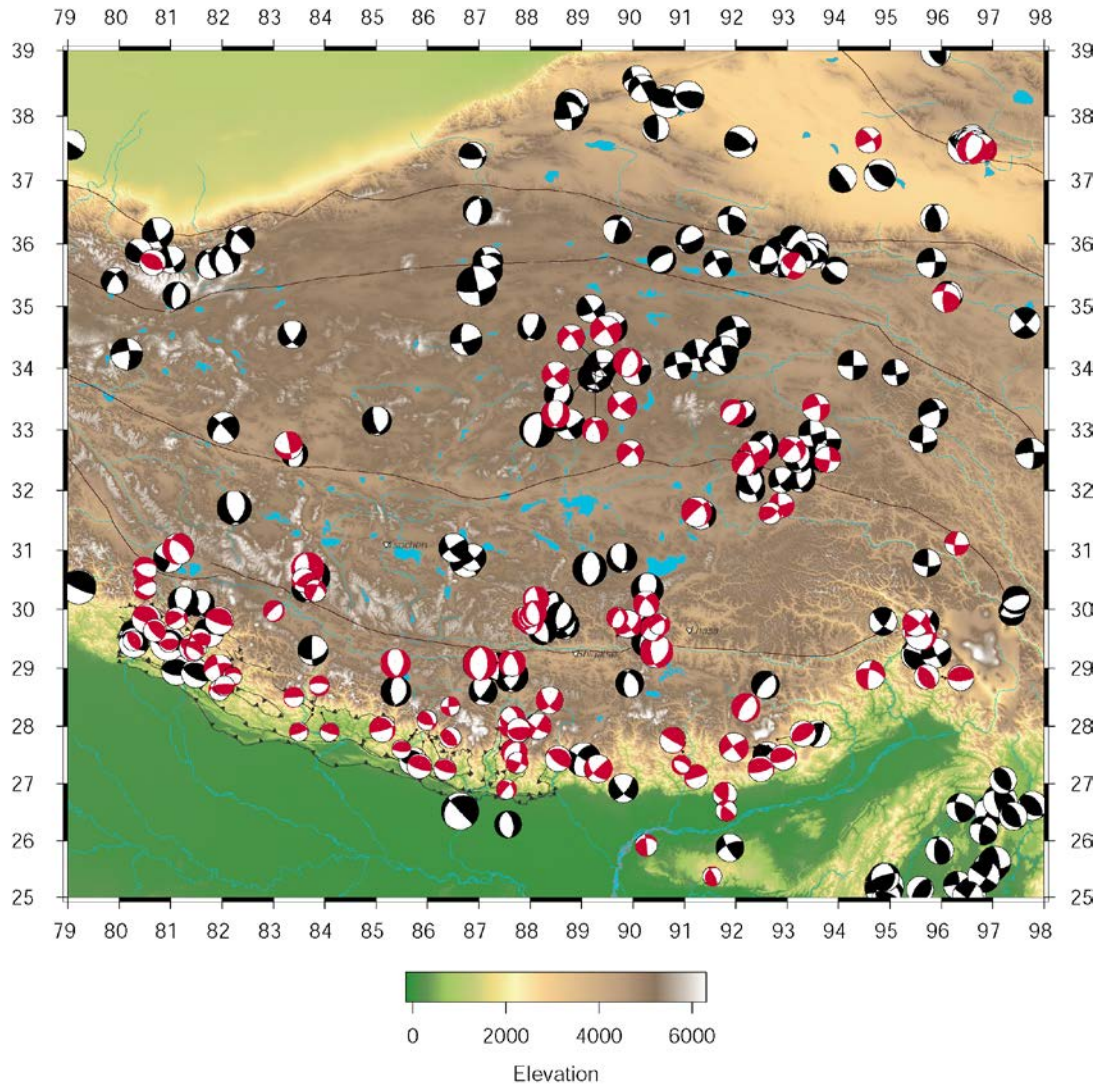


Figure 16. Regional moment tensor solutions. (From Monigle, et al., 2012 and after Burtin, 2005 and Baur, 2007.) We analyzed 143 seismic events in Nepal and southern Tibet using high-quality broadband waveforms. The Hi-CLIMB set of 115 solutions contains events as small as $M_w=3.5$. In southern Tibet and Nepal our efforts substantially expand the moment-tensor catalog.

The Hi-CLIMB data allow analysis of smaller $M_w \geq 3.5$ events with near-regional seismograms at periods of $T \geq 15-20$ s (Baur, 2007; Monigle, et al., 2012). We obtained 115

moment tensors. High quality and redundancy of the data allow parameter resolution tests for size, depth, and moment tensor. For the PXR events (near 30°N, 88°E), where we have good event location control (Monigle, et al., 2012), a significant number of events with similar-looking waveforms spanning a wide size range and good recording geometry allowed testing of parameter resolution and evaluating of velocity-depth models for seismogram calculation. The tests suggest a depth resolution for shallow crustal events on the order of ± 5 km, an estimated M_w uncertainty of ± 0.1 – 0.2 units, and uncertainties for strike, dip, and rake on the order of 5° – 10° with currently used velocity models and event locations.

Table 1. 143 regional moment tensor solutions in Nepal and southern Tibet. *S/D/R* are strike, dip and rake of one nodal plane; *CD* is centroid depth; M_w is moment magnitude, *DC* is double-couple percentage of deviatoric moment tensor; *ST* is number of stations used for inversion; *Aut* designates author, *Bu*: Burtin, 2005, *Ba*: Baur, 2007, *Mo*: Monigle, et al., 2012.

Event ID YrMoDa_HrMi	Lat (°)	Lon (°)	S/D/R (°/°/°)	CD (km)	M_w	DC (%)	ST (#)	Aut
880820_2309	26.755	86.616	317/89/-111	52	6.7	100	2	Bu
881029_0910	27.871	85.648	284/53/87	21	5.1	53	2	Bu
911209_0102	29.543	81.632	114/53/83	17	5.0	64	9	Bu
911221_1952	27.795	87.955	212/88/13	66	4.9	57	4	Bu
920206_0335	29.61	95.521	204/63/87	11	5.2	47	6	Bu
920404_1743	28.147	87.979	145/66/-153	55	5.0	41	7	Bu
920602_2207	28.984	81.913	346/79/-151	53	5.2	61	10	Bu
920730_0824	29.584	90.163	174/60/-117	9	6.1	90	2	Bu
930320_1451	29.084	87.333	359/53/-95	13	6.3	67	3	Bu
930331_1344	29.091	87.349	336/61/-124	16	5.1	85	3	Bu
930524_0502	28.835	96.082	87/72/90	22	4.9	55	7	Bu
950217_0244	27.635	92.371	238/76/18	25	5.3	100	6	Bu
960426_1630	27.825	87.821	84/79/-112	75	4.7	93	1	Bu
960609_2325	28.325	92.201	210/65/-85	80	5.3	79	4	Bu
960925_1741	27.433	88.552	140/70/105	25	4.8	70	5	Bu
961120_2327	28.853	96.021	321/55/83	33	4.7	14	2	Bu
970105_0847	29.845	80.532	108/71/79	17	5.4	64	6	Bu
970718_1939	26.811	91.793	7/66/139	27	4.5	93	3	Bu
971030_0202	29.552	89.698	143/87/-142	94	5.3	82	3	Bu
971103_0229	29.078	85.383	162/48/-110	11	5.5	96	7	Bu
980708_0344	27.325	91.027	73/85/101	10	4.6	71	6	Bu
980818_0410	27.55	90.977	121/87/85	21	4.8	95	4	Bu
980926_1827	27.77	92.812	60/58/95	16	4.9	86	4	Bu
981126_1014	27.753	87.894	19/58/-106	57	4.8	62	1	Bu
000102_1023	27.559	92.498	74/75/77	15	4.8	57	3	Bu
000125_1643	27.663	92.631	69/67/71	13	4.8	67	2	Bu
010927_2240	26.817	87.593	50/54/-53	27	3.8	75	5	Ba
011106_1409	27.268	91.919	79/68/87	15	4.5	72	12	Ba

011107_0458	29.99	85.6*	349/54/-101	22	4.1	84	9	Ba
011127_0731	29.606	81.752	109/77/85	15	5.3	64	4	Bu
011202_2241	27.15	88.171	117/56/124	15	4.8	89	13	Ba
011218_0222	29.612	81.78	135/68/96	21	4.0	72	6	Ba
020307_1550	29.56	84.83*	137/89/-121	77	4.2	97	9	Ba
020323_0456	29.863	87.928	189/57/-65	7	4.5	72	11	Ba
020402_1957	29.287	87.009	221/80/-43	18	3.5	47	9	Ba
020508_1756	28.659	86.584	232/73/30	77	3.8	97	6	Ba
020509_0109	29.826	87.837	182/53/-67	6	4.1	78	13	Ba
020604_1436	30.595	81.44	326/82/-117	15	5.6	99	6	Ba
020604_1727	30.425	81.398	324/75/-46	27	4.3	48	10	Ba
020606_0135	30.457	81.251	306/87/-120	18	4.2	88	3	Ba
020620_0540	26.25	89*	148/85/162	30	4.6	100	13	Ba
020702_1710	27.11	84.78*	173/74/-148	70	3.9	66	6	Ba
020709_0308	29.889	87.995	325/61/-112	6	4.4	94	10	Ba
020716_1839	27.774	87.468	192/58/-69	65	3.8	77	7	Ba
020718_2324	28.2	87.927*	356/87/-37	78	3.7	48	6	Ba
020806_2330	29.912	87.87	332/47/-108	6	4.4	86	13	Ba
020822_0450	29.818	88.087	321/71/-107	9	4.3	93	16	Ba
020831_1240	29.92	88.12*	328/70/-106	5	4.6	91	23	Ba
020927_1714	33.364	93.567	254/79/-25	39	5.1	85	10	Ba
021019_0724	35.654	93.129	210/89/-150	36	4.9	89	3	Ba
021026_2028	35.141	96.097	183/72/141	21	5.4	81	8	Ba
021104_1059	28.855	82.208	262/59/-122	24	3.5	99	8	Ba
021116_0852	29.667	90.409	225/64/-59	16	4.4	83	15	Ba
021129_1649	29.676	90.395	235/64/-54	16	4.7	97	25	Ba
030116_1136	29.8	88.006	339/48/-113	3	4.8	61	11	Ba
030116_2215	32.615	89.948	227/89/-29	25	5.0	95	10	Ba
030118_1031	28.622	81.95	120/58/117	33	3.8	76	7	Ba
030131_0604	29.746	90.515	240/69/-49	10	4.0	74	9	Ba
030211_1036	32.512	93.787	98/86/-164	27	4.8	50	2	Ba
030226_1958	28.347	86.449	180/72/-160	75	3.9	93	8	Ba
030325_1851	27.264	89.331	229/87/23	32	5.5	100	13	Ba
030331_0532	26.528	91.827	307/74/45	65	3.9	58	4	Ba
030520_1834	32.681	93.094	226/82/-37	21	5.1	70	17	Ba
030524_1127	32.588	92.425	214/56/-79	12	4.5	82	2	Ba
030524_1932	32.609	92.337	334/86/174	36	4.9	75	9	Ba
030529_1418	35.705	80.653	110/50/79	21	4.8	39	4	Ba
030707_0655	34.606	89.475	327/80/-168	21	5.8	60	14	Ba
030708_1230	26.905	87.546	222/79/-53	12	3.7	15	12	Ba
030728_0245	28.698	82.045	108/82/79	15	3.7	21	10	Ba
030818_0903	29.573	95.605	250/90/-45	24	5.7	46	16	Ba
030929_1340	27.358	87.738	69/71/45	12	4.0	66	15	Ba
031028_0231	32.446	92.173	217/76/-70	7	4.8	39	16	Ba
031122_0507	28.277	83.767	265/88/-94	16	3.8	87	22	Ba

031122_2331	28.202	83.767	71/82/81	21	3.5	84	29	Ba
031123_1915	28.297	83.773	270/77/-87	14	3.7	89	17	Ba
031210_1717	30.469	83.278	307/82/-108	30	4.3	94	11	Ba
031212_1339	37.626	94.588	59/81/24	25	4.8	98	18	Ba
040103_1314	27.739	85.931	109/75/87	14	4.7	96	25	Ba
040106_0313	30.539	86.042	18/83/-16	22	4.6	97	4	Ba
040210_0539	32.745	83.301	333/65/-110	29	4.6	24	11	Ba
040218_0123	27.361	87.758	291/82/160	24	3.9	75	23	Ba
040224_2021	37.487	96.828	144/80/-166	17	4.9	57	19	Ba
040227_1253	28.127	87.66	108/54/-133	92	4.6	80	21	Ba
040301_1741	30.368	80.496	241/65/-128	23	4.2	93	19	Ba
040306_1154	33.291	91.953	31/56/-108	5	4.7	67	5	Ba
040307_1329	31.639	91.236	228/80/-54	11	5.6	81	9	Ba
040316_2123	37.558	96.668	151/69/151	11	4.9	35	5	Ba
040327_1847	33.954	89.179	26/51/-60	8	5.8	93	11	Ba
040327_2005	33.931	89.292	353/63/-126	9	4.4	83	5	Ba
040328_2205	34.132	89.275	324/76/-159	23	4.9	41	7	Ba
040328_2227	33.957	89.265	337/68/-130	15	4.8	29	7	Ba
040403_0251	29.846	81.118	309/62/127	74	4.1	77	4	Ba
040422_1002	33.998	89.218	26/53/-56	5	5.2	50	10	Ba
040504_0504	37.506	96.758	56/83/-33	28	5.4	89	6	Ba
040510_2327	37.485	96.6	56/59/66	12	5.6	71	14	Ba
040523_0738	34.079	89.285	229/78/13	16	5.3	78	7	Ba
040523_1446	34.08	89.32	233/88/16	20	5.0	65	9	Ba
040605_0847	29.86	89.698	208/62/-70	9	3.9	72	3	Ba
040624_1003	29.868	87.905	14/54/-76	6	4.1	54	14	Ba
040630_1533	30.017	88.097	183/32/-79	12	4.2	83	54	Mo
040701_1914	30.016	88.082	177/30/-92	12	3.5	95	24	Mo
040703_1410	34.093	89.349	204/64/-80	10	5.4	83	14	Ba
040708_2149	30.032	88.161	191/33/-70	12	4.1	99	21	Mo
040711_2308	30.694	83.672	348/49/-90	16	6.2	47	17	Ba
040712_1438	30.746	83.773	31/80/-39	25	4.6	42	23	Ba
040715_2339	30.026	88.173	183/30/-81	12	3.4	90	45	Mo
040716_2033	28.232	83.944	108/81/92	10	3.6	73	14	Ba
040720_0335	27.938	85.793	94/73/95	13	3.6	89	12	Ba
040721_1544	30.035	88.150	183/29/-79	12	3.7	83	58	Mo
040723_0125	30.013	88.155	179/30/-78	12	4.5	84	83	Mo
040728_2222	30.714	83.633	2/70/-87	10	5.1	96	9	Ba
040804_0209	25.923	90.262	353/89/54	53	4.1	26	18	Ba
040821_0907	30.037	88.159	177/30/-85	12	4.5	94	81	Mo
040824_1005	32.542	92.19	326/83/165	12	5.3	61	10	Ba
040903_1024	30.033	88.150	176/25/-77	12	3.5	51	23	Mo
040909_0555	29.466	80.281	147/55/88	6	3.8	18	12	Ba
040912_0848	29.502	81.575	127/56/121	21	3.9	94	10	Ba
040915_1310	30.045	88.159	180/26/-78	12	3.8	77	56	Mo

040923_1728	31.116	96.308	94/80/-16	31	4.4	92	9	Ba
040927_1705	29.773	95.515	311/76/160	23	5.0	86	13	Ba
041001_1803	30.046	88.156	175/22/-94	15	3.4	57	32	Mo
041026_0211	31.024	81.154	187/62/-35	13	5.4	36	14	Ba
041026_1113	31.754	92.893	76/89/-16	25	4.7	67	27	Ba
041104_1400	30.056	88.161	164/32/-97	12	3.7	79	45	Mo
041110_0421	27.929	87.778	263/69/79	66	4.4	52	12	Ba
041124_2235	27.329	90.944	76/88/92	10	3.6	66	5	Ba
050108_1251	29.925	88.338	96/79/-179	15	3.2	87	11	Mo
050115_2232	29.439	80.965	263/62/80	22	3.7	84	13	Ba
050116_0843	29.646	80.696	140/71/101	10	4.3	76	26	Ba
050208_0151	27.82	86.033	99/57/50	20	3.8	98	22	Ba
050208_0335	27.738	86.092	108/75/89	10	4.1	44	30	Ba
050208_0413	27.76	86.072	325/59/102	21	3.9	73	10	Ba
050227_1832	25.371	91.553	332/73/69	19	3.5	77	8	Ba
050407_0140	29.299	81.451	300/74/-107	23	3.6	78	10	Ba
050407_2004	30.491	83.662	349/56/-95	8	6.3	79	21	Ba
050407_2141	30.588	83.681	355/52/-91	10	5.3	98	28	Ba
050408_1045	29.977	83.012	226/72/-85	10	4.0	76	10	Ba
050409_0920	30.494	83.599	230/61/59	34	4.4	49	15	Ba
050508_1642	30.097	90.261	317/66/-149	98	4.8	97	17	Ba
050511_0412	30.671	85.244	321/81/-166	4	4.4	82	70	Mo
050515_1921	31.613	92.676	55/67/52	35	4.2	91	16	Ba
050522_1417	30.319	83.822	25/88/46	12	4.0	95	10	Ba
050601_2006	28.881	94.626	283/88/-96	17	5.5	48	14	Ba

6. PUBLISHED RESULTS AND ONGOING RESEARCH

6.1. Low Angle Normal Faulting in the PXR

Seismicity north of the Yarlung-Tsangpo Suture in the Lhasa Terrane of southern Tibet occurs primarily along N-S trending grabens. Analysis concentrated on seismicity along the Pumqu-Xianza Rift (PXR) during July 2004 to June 2005 when close sites T0370 and T0320 were operating (Figure 17). The database contains about 350 events with 25 or more automatic picks slightly west of the PXR compared to 11 events, ranging in magnitude (m_b) from 4.0 to 4.8, listed in the USGS NEIC catalog. We relocated the 40 largest events ($M_L(P) \geq 3.2$) using manual P and S picks. Our database also includes events near T0370 and T0320 (Figure 17). We selected 10 stronger events ($2.1 \leq M_L(P) \leq 3.4$) to verify their locations; six satisfy GT5-criteria (Table 2, marked “&”).

A detailed description of the analysis, including manual earthquake locations, regional moment tensors, and a discussion of the mechanics involved in 30° low-angle normal faulting has been published in Monigle, et al., 2012. Here we report only on earthquake location and source aspects relevant to this project.

Automated locations with local Hi-CLIMB stations reveal a systematic west-southwest bias of routine NEIC epicenters that can reach ~50 km (Figure 17). Hi-CLIMB locations based on automatic P and S picks are closer to the rift and cluster near the central PQX. Manual phase picking for selected events verified the high automatic location quality with epicenter differences of only a few kilometers (Figure 17).

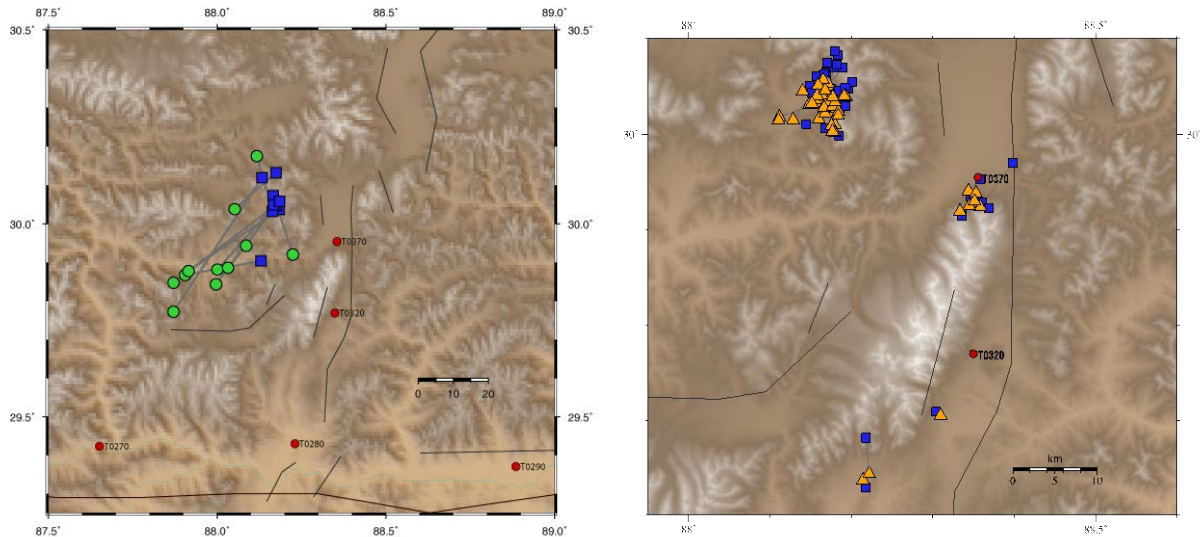


Figure 17. Left. Comparison of NEIC (green circles) and automated Hi-CLIMB (blue squares) seismic event locations for the PXR reveals a general SW NEIC location bias that can reach more than 40 km (average value for 11 common events is 25 km).

Figure 17. Right. Automatic (blue) and manual (orange) locations for 50 PXR events differ on average by less than 2 km and differences do not exceed 8 km. *The main northern cluster lacks azimuthal coverage to satisfy GT5 criteria.*

The manual locations of the main northern group cluster tightly west of the central PXR (Figure 17 and 18) and at about 10 km depth. The hypocenters are constrained by phase picks from close stations and are consistent with ~12 km depth (uncertainties of about ± 3 km) estimated from moment tensor analysis (Monigle, et al., 2012). All main cluster mechanisms are consistent with N-S oriented normal faulting on a $\sim 30^\circ$ west-dipping fault. This cluster technically does not satisfy GT5 criteria (e.g., Bondar, et al., 2004), even though the closest site is ~ 20 km from the epicenters, because of the large $\sim 150^\circ$ azimuthal gap since the events occurred at the northern terminus of the lateral array.

The seismic events south of T0370 are within the network and satisfy the azimuthal and close-distance-recording criteria for GT5; however, the events are smaller, ultimately only 6 satisfy the distance requirement. The largest event of the cluster just south of T0370 has a strike-slip mechanism and its waveform modeling depth is consistent with its hypocenter depth.

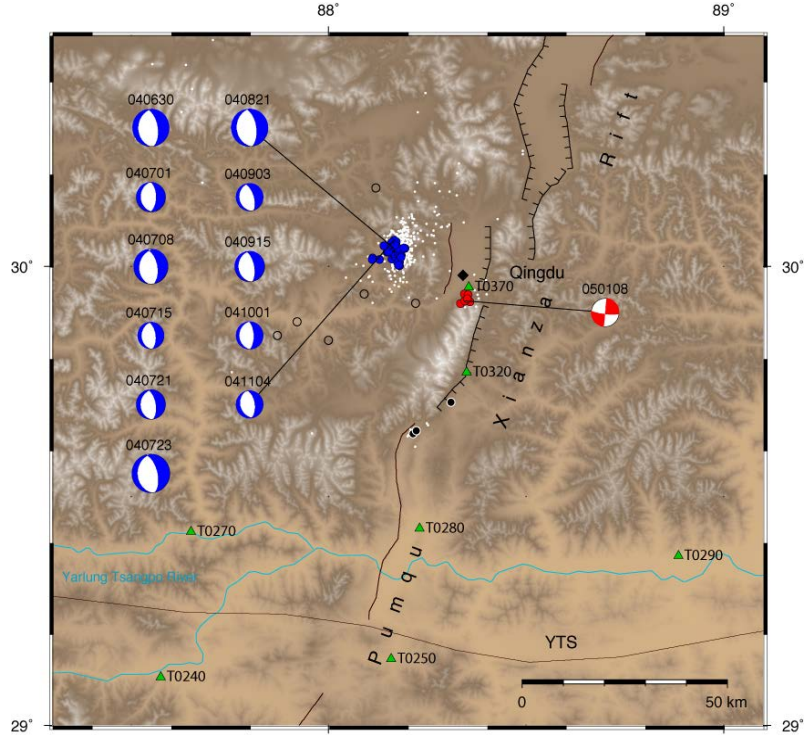


Figure 18. Map of the central PXR showing manual locations for 50 events. *Blue are events west of the rift, red near station T0370 and black south of T0320. White dots are epicenters from automatic picks (Carpenter, et al., 2010). Green triangles are Hi-CLIMB stations. Diamond is town of Qingdu. Open circles are NEIC locations for 6 events that all relocated into the blue cluster. Fault plane solutions from moment tensor analysis are given by event date (YYMMDD). After Monigle, et al., 2012.*

6.2. Velocity and Attenuation Tomography

In addition to the immediate deliverables of this project, our current work is focused on obtaining 3D P- and S-wave velocity structure from inversion of local and near-regional body waves and on inverting for the crust and upper mantle attenuation properties (Q). Both projects are performed by graduate students and planned to be completed in the near future.

6.2.1 Velocity Tomography

Resolving 3D P- and S- wave velocity and structure of the south-central Tibetan Plateau is the focus of a tomography effort aimed at complementing and expanding on the existing receiver function image of the collision zone (Nábělek, et al., 2009). We are using the tomoDD double-difference tomography code (Zhang and Thurber, 2003) and have begun with synthetic data inversions to evaluate how well our existing P and S wave dataset is able to resolve 3D crust and upper mantle structure considering the actual station and event distribution.

Our dataset consists of the P and S picks from the 5790 seismic events described in section 4.2 for which we have at least 15 P or S arrivals, which occurred within 2° from the closest Hi-CLIMB station, and have a minimum magnitude of $M_L(P) \geq 2.0$ to ensure significant path lengths.

These criteria result in more than 200,000 P picks and, due to the newly implemented polarization S picker, in more than 90,000 S arrivals providing dense ray coverage over the study area to invert for a high-resolution regional velocity structure. We are particularly excited about our S arrival dataset, which allows a joint inversion for P- and S-wave structure providing important compositional constraints.

6.2.2 Attenuation Tomography

Resolving the 3D attenuation structure (Q) of the south-central Tibetan Plateau is the focus of a second tomography project. Estimating 3D Q structure from t^* measurements is widely applied (e.g., Hauksson and Shearer, 2006). Our initial efforts had focused on estimating the resolving power of our dataset to invert event-station specific t^* values for 3D Q structure considering limited ray coverage in the lower part of the ~ 70 -km thick crust and in the uppermost mantle (through P_n and mantle P) beneath Tibet. Currently, we are working on optimizing unbiased t^* estimation from windowed body wave phases; work is performed using synthetic (spikes as well as full waveform synthetic seismograms) and real data. Once we obtain good t^* estimates, inverting for Q will be fast since the tomography procedures are already in place.

7. GT5 DATASET

We applied the Bondar, et al., 2004 criteria to identify candidate events for the seismic event ground truth (GT) database. 54 events from the 5790 event database described in section 4.2, which is based on STA/LTA P picks and polarization S picks, satisfied the GT5_{95%}-level criteria and were above an $M_L(P) \geq 2.0$ threshold. Arrival times for all 54 events were manually re-picked from three-component seismograms and then the events were relocated. We applied the P distance weighting described in section 4.1 to both P and S phases. The location results contain 51 events recorded by 10 or more stations within 250 km distance, with an azimuthal gap of 110° or less, at least one station within 30 km from the epicenter, and a secondary azimuthal gap of 160° or less. After manual relocation, a small shift in the epicenter resulted in two events not meeting the azimuthal gap criterion and one event was found to be much smaller than $M_L(P)=2.0$ and could not be picked reliably. Of the 51 events, 41 are at GT5_{95%}-level with records extending as P/P_n beyond the 250 km distance. The remaining 10 events are generally smaller; 9 of them satisfy GT5_{95%}-level criteria but lack distant detections and one event lacks distant arrivals and does not satisfy the secondary azimuthal requirement. All 51 events are shown in Figure 19. Table 2 includes all 41 GT5_{95%} (candidate) events.

For event #19, moment tensor inversion resulted in a double-couple strike-slip source mechanism at 15 km depth with roughly N-S and E-W trending nodal planes (Monigle, et al., 2012). Parameter uncertainties ($\sim 20^\circ$ for strike, dip, and rake and ± 10 km for depth) are large due to small event size ($M_w=3.2$, $M_L(P)=3.1$). The only event listed in the USGS NEIC and the ISC catalogs is event #32. The NEIC and ISC locations are about 13 km and over 30 km, respectively, south-southwest of our location. Manual locations with Hi-CLIMB data (ours and Griffin, et al., 2011) are within a few km of the automated location. Moment tensor analysis reveals a well-constrained double-couple strike-slip mechanism at 4 km depth with an E-W trending σ_3 -axis. Magnitude estimates for the event are similar ($M_L(P)=4.7$, $M_w=4.4$ vs. $m_b(\text{NEIC})=4.6$ and $m_b(\text{ISC})=4.3$).

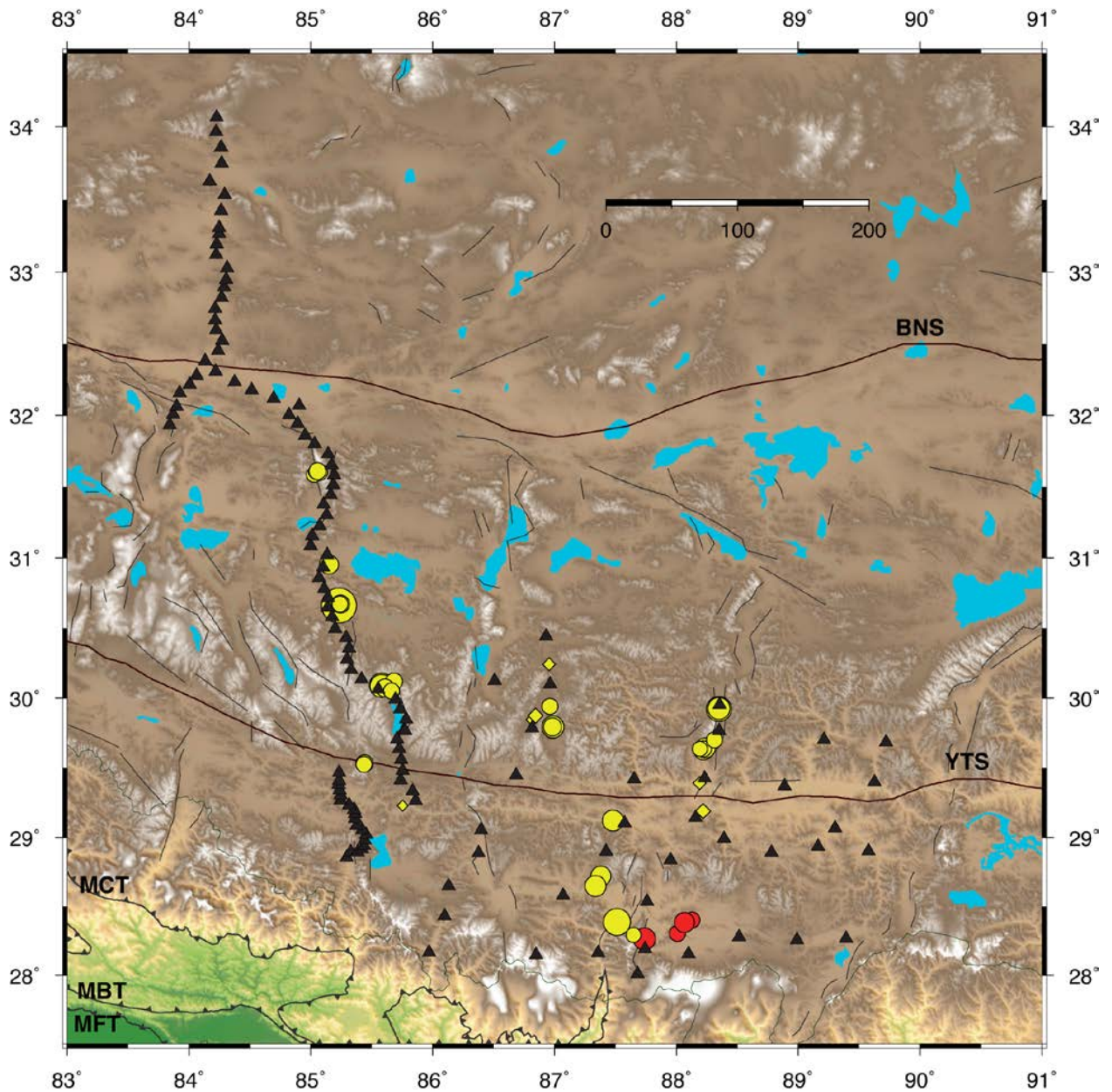


Figure 19. Map of 41 GT5_{95%} candidate events (circles). *Diamonds are 10 other candidates (all lack P/P_n beyond 250 km distance; all except one satisfy the secondary gap criterion). Shown are potentially monitoring relevant events with $M_L(P) \geq 2.0$ that can be detected several hundred km from a seismic event source. Color as in Figure 6.*

Table 2. Manual locations of 41 GT5_{95%} (candidate) events. “&” are PXR events. Moment tensor analysis was performed for events #19 and #32.

Event (#)	Date (M/D/Y)	Time (UTC)	Latitude (°N)	Longitude (°E)	Depth (km)	M _L (P)
1	06/17/04	07:00:23.7	31.607	85.066	6.3	2.2
2	06/26/04	01:26:36.7	31.590	85.026	0.7	2.0
3	07/02/04	00:45:10.7	31.608	85.043	0.7	2.0
4	07/02/04	01:00:09.4	31.611	85.057	0.9	2.3
5	07/22/04	17:34:29.7	28.403	88.129	72.0	2.1
6	08/02/04	21:48:29.6	28.305	88.009	75.1	2.2
7	08/05/04	19:09:26.9	29.775	86.985	10.8	2.3
8	08/13/04	17:10:42.5	29.124	87.482	4.0	2.8
9	08/16/04	10:20:54.8	29.535	85.442	0.8	2.3
10	08/16/04	13:46:55.2	29.528	85.437	10.6	2.1
11	09/04/04	17:36:54.2	30.100	85.580	7.0	3.2
12	09/15/04	04:36:26.6	30.092	85.581	10.5	3.1
13	10/22/04	03:28:42.5	28.722	87.381	0.9	2.7
14	12/08/04	22:48:37.3	29.796	86.987	0.3	3.0
15	12/08/04	22:57:20.1	29.799	86.984	3.9	2.4
16	12/15/04	00:03:07.0	28.387	88.067	72.1	2.6
17&	01/01/05	22:46:22.4	29.927	88.349	8.2	3.4
18&	01/04/05	00:30:48.9	29.950	88.349	9.7	2.3
19&	01/08/05	12:51:09.7	29.929	88.350	9.4	3.0
20	02/16/05	02:33:55.6	30.953	85.150	5.1	2.6
21&	02/20/05	23:41:13.0	29.643	88.219	0.0	2.2
22&	02/22/05	23:38:26.5	29.630	88.224	0.0	2.5
23&	02/23/05	02:03:45.6	29.640	88.228	0.6	1.9
24&	02/23/05	03:30:09.2	29.648	88.241	0.7	2.6
25&	02/23/05	19:53:04.1	29.639	88.222	0.0	2.2
26	03/19/05	09:30:47.0	29.945	86.964	7.0	2.2
27&	04/30/05	03:43:10.7	29.639	88.193	0.3	2.1
28	05/03/05	08:51:23.6	28.266	87.737	80.8	3.0
29	05/10/05	21:47:53.2	28.649	87.339	4.7	2.5
30	05/11/05	00:45:35.5	30.672	85.235	8.7	2.8
31	05/11/05	01:51:48.7	30.667	85.228	12.2	2.1
32	05/11/05	04:13:00.2	30.665	85.232	5.8	4.7
33	05/11/05	06:37:07.2	28.648	87.338	8.5	2.8
34	05/11/05	08:25:44.6	30.673	85.243	7.1	2.5
35&	06/04/05	20:44:15.6	29.706	88.314	0.5	2.2
36	06/09/05	18:53:58.8	30.125	85.684	0.7	2.2
37	06/16/05	18:34:32.1	28.295	87.648	65.2	2.0
38	07/06/05	03:11:02.7	28.388	87.512	69.6	3.6
39	07/28/05	00:21:37.9	30.076	85.609	10.6	2.4
40	07/29/05	05:06:03.0	30.674	85.239	12.6	2.1
41	08/15/05	10:13:46.2	30.054	85.662	8.0	2.2

8. CONCLUSIONS

- The Hi-CLIMB broadband seismic dataset provides the opportunity for ground truth location and source parameter determination in an important region.
- The dataset reveals an abundance of seismic events not included in any other catalog. We developed modules to clean up the automatic event location database that eliminate spurious phase arrivals leading to improved locations, or, where this was impossible, remove spurious events entirely. The resulting database contains over 22,500 events with over 7,900 based on 25 or more P and S arrivals. Manual locations of a small subset of events in southern Tibet reveal a non-systematic, few-kilometer-scale difference between locations based on automatic and manual phase picks. Applying additional requirements on the station distribution results in a high-quality subset of events with resolved hypocenters that show a bimodal depth distribution with events occurring shallower than 20 km and at the Moho and deeper.
- Initial M_L determination indicated systematic underestimation and frequent contamination of smaller events by later, larger events due to the high level of seismicity. Instead of determining M_L from S phases, we implemented a local magnitude based on P wave amplitudes $M_L(P)$ and use a simple, physics-based conversion to obtain regular M_L .
- S-picker. During the last reporting period, our focus was on the implementation of an automatic S-phase picker, which uses polarization characteristics specifically geared towards detecting shear wave signals and performs superior to a standard STA/LTA detector in terms of number of detections and pick accuracy. After optimizing picking parameters and threshold settings to our dataset, we applied the polarization S picker to all Hi-CLIMB events of magnitude greater than 2.
- Waveform modeling efforts resulted in a 143 event moment tensor database.
- We identified 54 GT5-candidate events with $ML(P) \geq 2.0$ of which 50 satisfy the GT5 criteria at the 95% confidence level.
- Two studies that are close to finishing will lead to further improvements in event location and characterization through tomographic imaging and attenuation analysis.
- The GT5 locations and moment tensor depths will contribute to SLBM tomographic efforts, allow evaluation of depth for crustal models, and enhance model accuracy throughout central and southern Asia and, in general, will contribute to the National Nuclear Security Administration (NNSA) Knowledge Base.

REFERENCES

- Baur, J., 2007, Seismotectonic analysis of the Himalayan-Tibetan collision zone from regional seismic moment tensor analysis with Hi-CLIMB data, *M.Sc. thesis, Oregon State University, Corvallis, Oregon*.
- Bondar, I., S. C. Myers, E. R. Engdahl, and E. A. Bergman, 2004, Epicentre accuracy based on seismic network criteria, *Geophys. J. Int.*, **156**, pp. 483-496, doi: 10.1111/j.1365-246X.2004.02070.x.
- Braunmiller, J., N. Deichmann, D. Giardini, W. Wiemer, and the SED Magnitude Working Group, 2005, Homogeneous moment-magnitude calibration in Switzerland, *Bull. Seis. Soc. Am.*, **95**, pp. 58-74, doi: 10.1785/0120030245.
- Burtin, A., 2005, Seismotectonics of the Himalayan arc from regional seismogram moment tensor inversion, *Internship Report, Oregon State University, Corvallis, Oregon*.
- Burtin, A., J. Nabelek, J. Baur, and J. Vergne, 2005, Evidence for the decoupling of stress above and beneath the Main Himalayan Thrust, *Eos Trans. Am. Geophys. Union* 86(52): Fall Meet. Suppl., Abstract T43A-1379.
- Carpenter, S., 2010, South-central Tibetan seismicity recorded by HiCLIMB seismic array, *M.Sc. thesis, Oregon State University, Corvallis, Oregon*.
- Carpenter, S., J. Nábělek, and J. Braunmiller, 2010, South-central Tibetan seismicity from HiCLIMB seismic array data, *Eos Trans. Am. Geophys. Union*, 91 (52), Fall Meet. Suppl., Abstract T43B-2223.
- Cichowicz, A., 1993, An automatic S-phase picker, *Bull. Seismol. Soc. Am.*, **83**, pp. 180-189.
- De la Torre, T. L., G. Monsalve, A. F. Sheehan, S. Sapkota, and F. Wu, 2007, Earthquake processes of the Himalayan collision zone in eastern Nepal and the southern Tibetan Plateau, *Geophys. J. Int.*, **171**, pp. 718-738, doi: 10.1111/j.1365-246X.2007.03537.x.
- Diehl, T., N. Deichmann, E. Kissling, and S. Husen, 2009, Automatic S-wave picker for local earthquake tomography, *Bull. Seismol. Soc. Am.* **99**, pp. 1906-1920, doi: 10.1785/0120080019.
- Elliot, J. R., R. J. Walter, P. C. England, J. A. Jackson, Z. Li, and B. Parsons, 2010, Extension on the Tibetan plateau: Recent normal faulting measured by InSAR and body wave seismology, *Geophys. J. Int.*, **183**, pp. 503-535, doi: 10.1111/j.1365-246X.2010.04754.x.
- Griffin, J. D., R. L. Nowack, W.-P. Chen, and T.-L. Tseng, 2011, Velocity structure of the Tibetan lithosphere: Constraints from P-wave travel times of regional earthquakes, *Bull. Seismol. Soc. Am.*, **101**, pp. 1938-1947.
- Hauksson, E. and P. Shearer, 2006, Attenuation models (Q_P and Q_S) in three-dimensions of the Southern California crust: Inferred fluid-saturation at seismogenic depths, *J. Geophys. Res.*, **111**, B05302, doi: 10.1029/2005JB003947.
- Langin, W. R., L. D. Brown, and E. A. Sandvol, 2003, Seismicity of central Tibet from project INDEPTH III seismic recordings, *Bull. Seismol. Soc. Am.*, **93**, pp. 2146-2159.

- Liang, X., S. Zhou, Y. J. Chen, G. Jin, L. Xiao, P. Liu, Y. Fu, Y. Tang, X. Lou, and J. Ning, 2008, Earthquake distribution in southern Tibet and its tectonic implications, *J. Geophys. Res.*, **113**, B12409, doi: 10.1029/2007JB005101.
- Monigle, P. W., J. Nábělek, J. Braunmiller, and N. S. Carpenter, 2012, Evidence for low-angle normal faulting in the Pumqu-Xianza Rift, Tibet, *Geophys. J. Int.* doi: 10.1111/j.1365-246X.2012.05581.x.
- Monsalve, G., A. Sheehan, V. Schulte-Pelkum, S. Rajaure, M. R. Pandey, and F. Wu, 2006, Seismicity and one-dimensional velocity structure of the Himalayan collision zone: Earthquakes in the crust and upper mantle, *J. Geophys. Res.*, **111**: B10301, doi: 10.1029/2005JB004062.
- Nábělek, J. and G. Xia, 1995, Moment-tensor analysis using regional data: Application to the 25 March, 1994, Scotts Mills, Oregon earthquake, *Geophys. Res. Lett.*, **22**, pp. 13-16.
- Nábělek, J., J. Vergne, G. Hetenyi, and the Hi-CLIMB Team, 2005, Project Hi-CLIMB: A synoptic view of the Himalayan collision zone and southern Tibet, *Eos Trans. Am. Geophys. Union* 86(52): Fall Meet. Suppl., Abstract T52A-02.
- Nábělek, J., G. Hetényi, J. Vergne, S. Sapkota, B. Kafle, M. Jiang, H. Su, J. Chen, B.-S. Huang, and the Hi-CLIMB Team, 2009, Underplating in the Himalaya-Tibet collision zone revealed by the Hi-CLIMB experiment, *Science*, **325**, p. 1371, doi: 10.1126/science.1167719.
- Zhang, H. and C. H. Thurber, 2003, Double-difference tomography: The method and its application to the Hayward Fault, California, *Bull. Seismol. Soc. Am.* **93**, pp. 1875-1889.
- Zhu, L. and D. V. Helmberger, 1996, Intermediate depth earthquakes beneath the India-Tibet collision zone, *Geophys. Res. Lett.*, **23(5)**, pp. 435-438.

LIST OF SYMBOLS, ABBREVIATIONS, AND ACRONYMS

AFRL	Air Force Research Laboratory
GSN	Global Seismic Network
GT	Ground truth
NEIC	National Earthquake Information Center
PXR	Pumqu-Xianza Rift
USGS	U.S. Geological Survey

DISTRIBUTION LIST

DTIC/OCP 8725 John J. Kingman Rd, Suite 0944 Ft Belvoir, VA 22060-6218	1 cy
AFRL/RVIL Kirtland AFB, NM 87117-5776	2 cys
Official Record Copy AFRL/RVBYE/Robert Raistrick	1 cy

This page is intentionally left blank.